Single-Cell Analysis of Refractory Celiac Disease Demonstrates Inter- and Intra-Patient Aberrant Cell Heterogeneity

Dieckman, Tessa ; Schreurs, Mette ; Mahfouz, Ahmed; Kooy-Winkelaar, Yvonne ; Neefjes-Borst, Andra ; Bouma, Gerd ; Koning, Frits

DOI
10.1016/j.jcmgh.2022.03.005

Publication date
2022

Document Version
Final published version

Published in
CMGH

cmgh
CELLULAR AND MOLECULAR GASTROENTEROLOGY AND HEPATOLOGY

ORIGINAL RESEARCH

Single-Cell Analysis of Refractory Celiac Disease Demonstrates Inter- and Intra-Patient Aberrant Cell Heterogeneity

Tessa Dieckman,[1,2] Mette Schreurs,[1] Ahmed Mahfouz,[3,4] Yvonne Kooy-Winkelaar,[1] Andra Neefjes-Borst,[5] Gerd Bouma,[2] and Frits Koning[1]

[1]Department of Immunology, Leiden University Medical Center, Leiden, The Netherlands; [2]Department of Gastroenterology and Hepatology, Amsterdam UMC, Vrije Universiteit Amsterdam, Amsterdam Gastroenterology Endocrinology Metabolism, Amsterdam, The Netherlands; [3]Pattern Recognition and Bioinformatics, Delft University of Technology, Delft, The Netherlands; [4]Department of Human Genetics, Leiden University Medical Center, Leiden, The Netherlands; [5]Department of Pathology, Amsterdam UMC, Vrije Universiteit Amsterdam, Amsterdam, The Netherlands

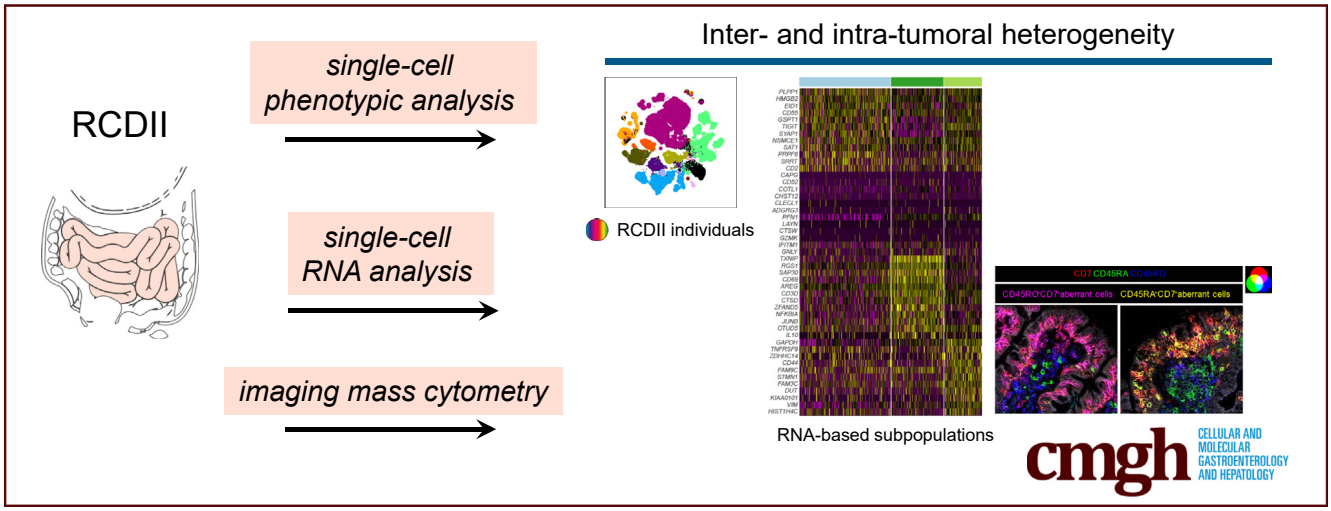

SUMMARY

Using high-dimensional single-cell and spatial technologies, we demonstrate substantial intertumoral and intratumoral heterogeneity of the aberrant cell population in patients with refractory celiac disease type II (RCDII). These findings may have implications for future diagnostics and treatment of RCDII.

BACKGROUND & AIMS: Refractory celiac disease type II (RCDII) is a rare indolent lymphoma in the small intestine characterized by a clonally expanded intraepithelial intracellular $CD3^+$surfaceCD3$^-$$CD7^+$$CD56^-$ aberrant cell population. However, RCDII pathogenesis is ill-defined. Here, we aimed at single-cell characterization of the innate and adaptive immune system in RCDII.

METHODS: Paired small intestinal and blood samples from 12 RCDII patients and 6 healthy controls were assessed by single-cell mass cytometry with a 39–cell surface marker antibody panel, designed to capture heterogeneity of the innate and adaptive immune system. A second single-cell mass cytometry panel that included transcription factors and immune checkpoints was used for analysis of paired samples from 5 RCDII patients. Single-cell RNA sequencing analysis was performed on duodenal samples from 2 RCDII patients. Finally, we developed a 40-marker imaging mass cytometry antibody panel to evaluate cell–cell interactions in duodenal biopsy specimens of RCDII patients.

RESULTS: We provide evidence for intertumoral and intratumoral cell heterogeneity within the duodenal and peripheral aberrant cell population present in RCDII. Phenotypic discrepancy was observed between peripheral and duodenal aberrant cells. In addition, we observed that part of the aberrant cell population proliferated and observed co-localization of aberrant cells with $CD163^+$ antigen-presenting cells (APCs) in situ. In addition, we observed phenotypic discrepancy between peripheral and duodenal aberrant cells.

CONCLUSIONS: Novel high-dimensional single-cell technologies show substantial intertumoral and intratumoral heterogeneity in the aberrant cell population in RCDII. This may underlie variability in refractory disease status between patients and responsiveness to therapy, pointing to the need for personalized therapy in RCDII based on patient-specific immune profiles. *(Cell Mol Gastroenterol Hepatol 2022;14:173–192; https://doi.org/10.1016/j.jcmgh.2022.03.005)*

Keywords: Tumor Heterogeneity; Mass Cytometry; Imaging Mass Cytometry; Gluten Enteropathy; Enteropathy-Associated T-Cell Lymphoma.

Celiac disease (CeD) is a frequently occurring immune-mediated disease with an increasing prevalence worldwide owing to improved recognition and plausibly an increase in environmental factors that trigger CeD.[1] CeD pathogenesis is induced by gluten peptides in HLA-DQ2/8 individuals, leading to villous atrophy and associated malabsorption.[2] In rare cases, CeD patients develop, or present with, an expansion of intraepithelial intracellular CD (iCD)3$^+$ surface CD (sCD)3$^-$CD7$^+$CD56$^-$ aberrant cells in their duodenum.[3] This disease entity is called type II refractory celiac disease (RCDII) and is categorized as a low-grade lymphoma.

Previously, we showed substantial heterogeneity within the intestinal innate lymphoid compartment and identified a likely precursor for the aberrant cells in RCDII that is common in the healthy intestine, particularly in children.[4] More recently, it has been shown that the aberrant clonal cell population develops from an atypical NKp44$^+$ innate intraepithelial lymphocyte (IEL) subset in healthy duodenum.[5] Triggers for initiation of this development are only hypothesized, namely silent chronic inflammation resulting from continuous interleukin (IL)15 exposure[5,6] or a viral trigger such as Epstein–Barr virus.[7] Moreover, in 50% of RCDII cases, an accumulation of *JAK1/STAT3* mutations contributes to transformation of atypical innate IELs into a clonal aberrant cell population.[5,8,9]

RCDII is seen as a severe complication of CeD because this patient population has a 50% risk of developing a high-grade, enteropathy-associated, T-cell lymphoma (EATL),[10] which has a 5-year survival rate of only 20%. Next to the risk of EATL development, the clinical status of RCDII patients can be life-threatening and patients often pass away because of refractory disease status with malabsorption. There is no consensus about treatment of RCDII patients, with expert opinion–based therapy differing per country. Ideally, adequate therapy controls small intestinal mucosal injury and reduces accompanying symptoms, in some cases along with the continued presence of an aberrant cell population. To improve clinical care for RCDII, more insight into the immunologic environment and mechanisms that cause immune dysregulation is required.

To obtain a better understanding of immune dysregulation in RCDII, we aimed to perform unbiased single-cell characterization of the innate and adaptive immune system in RCDII. Here, we present an integrated analysis of multidimensional single-cell data collected using single-cell mass cytometry, single-cell RNA sequencing (scRNA-seq), and imaging mass cytometry. Collectively, we provide evidence for intertumoral and intratumoral heterogeneity of the aberrant clonal cell population and observed phenotypic discrepancy between duodenal and peripheral aberrant cells. Moreover, we observed proliferation of a subset of aberrant cells and we show spatial distribution of innate and adaptive immune cells in RCDII duodenum.

Results

Generation of Single-Cell Mass Cytometry Data Sets

We designed 2 single-cell mass cytometry antibody panels (see the Methods section): the first panel was designed for analysis of 39 immune cell surface markers to capture heterogeneity within the innate and adaptive immune system; the second panel was designed for analysis of 42 intracellular and cell surface markers to capture expression of transcription factors and checkpoint molecules. For the first panel, we included paired small intestinal biopsy and blood samples from controls (healthy duodenum) (n = 6) and RCDII patients (n = 12 inclusions, 10 individual patients) (Table 1). For the second panel, we included paired small intestinal biopsy and blood samples of 5 RCDII patients (Table 1). For RCDII samples, active disease was characterized by aberrant IELs ≥20% plus malabsorption, and remission was characterized by aberrant IELs ±20% without malabsorption. Small intestinal biopsy samples were duodenum-derived, with one exception of a jejunal sample. From biopsy samples, we isolated and pooled IELs and lamina propria (LP) lymphocytes. From peripheral blood, we isolated peripheral blood mononuclear cells (PBMCs). After staining and measurement, we performed pregating of live single CD45$^+$ cells based on Gaussian parameters (see the Methods section; data not shown) and checked the consistency of antibody (Ab) staining in both panels (see the Methods section; data not shown). Panel 1 generated a data set of 1.8 × 10^6 duodenal CD45$^+$ cells from control and RCDII patients (Figure 1*A*); panel 2 resulted in a data set of 404,252 duodenal CD45$^+$ cells from RCDII patients (Figure 1*B*). From peripheral blood, for panels 1 and 2, we generated data sets of 7.1 × 10^6 CD45$^+$ cells and 2.4 × 10^6 CD45$^+$ cells (data not shown), respectively.

Identification of Known Duodenal Immune Subsets

To obtain an overview of the duodenal immune cell composition we performed an hierarchical stochastic neighborhood embedding (HSNE) analysis of our mass cytometry data[11] in Cytosplore (Delft, The Netherlands),[12] a visual dimensionality reduction-based technique. At

Abbreviations: **Ab, antibody; APC, antigen-presenting cell; CeD, celiac disease; Ctrl, control; CyTOF, cytometry by time-of-flight; DE, differentially expressed; EATL, enteropathy-associated T-cell lymphoma; FCS, fetal calf serum; GATA3, GATA Binding Protein 3; HSNE, hierarchical stochastic neighborhood embedding; iCD, intracellular CD; IEL, intraepithelial lymphocyte; IL, interleukin; ILC, innate lymphoid cell; LP, lamina propria; NK, natural killer; PBMC, peripheral blood mononuclear cell; PBS, phosphate-buffered saline; PCA, principal component analysis; RCDII, refractory celiac disease type II; ROI, region of interest; RORγT, retinoic acid receptor-related orphan receptor gamma T; sCD, surface CD; scRNA-seq, single-cell RNA sequencing; SMA, smooth muscle actin; TCR, T-cell receptor; TF, transcription factor; tSNE, t-distributed stochastic neighborhood embedding; TGF, transforming growth factor; UMAP, uniform manifold approximation and projection.**

Most current article

2352-345X
https://doi.org/10.1016/j.jcmgh.2022.03.005

Table 1. Patient Characteristics

	CyTOF panel 1		CyTOF panel 2	scRNA-seq
	Ctrl	RCDII	RCDII	RCDII
Inclusions, n	6	12	5	2
Patients, n	6	10	5	2
Sex, male:female, n	2:4	5:7	2:3	1:1
Age, median				
Time of endoscopy	54.5	78	79	75
CeD diagnosis	–	69.5	72	67
RCDII diagnosis	–	71	75	68
Years between CeD and RCDII diagnosis, median	–	1.5	3	1.5
CeD disease, *y*, median	–	6	5	8.5
Histology				
Marsh 0	6	3	0	1
Marsh 1	0	3	2	0
Marsh 2	0	0	0	0
Marsh 3A	0	5	2	1
Marsh 3B	0	0	0	0
Marsh 3C	0	1	1	0
% aIELs vs total IELs, median	-	71	69	72.5
(Previous) RCDII treatment, n				
No GFD	5	1	0	0
GFD	1	11	5	2
No drug treatment	0	3	1	0
Cladribine	0	5	2	0
Budesonide	0	0	1	0
Anti-IL15	0	0	0	0
Budesonide + anti-IL15	0	1	0	0
Cladribine + auSCT	0	2	0	0
Cladribine + auSCT + anti-IL15	0	1	1	1
Small jejunal resection + CHOEP chemotherapy	0	0	0	1
Disease status, n				
Active (aIELs >20% + malabsorption)	-	6	3	1
Remission (±aIEL > 20%, no malabsorption)	-	6	2	1
Samples, n				
PBMCs	6	9	5	0
Duodenum	6	11	5	2
Jejunum	0	1	0	0
Total	12	21	10	2

aIELs, aberrant intra-epithelial lymphocytes; auSCT, autologous stem cell transplantation; CeD, celiac disease; Ctrl, control; GFD, gluten-free diet; RCDII, refractory celiac disease type II.

overview HSNE level, we discriminated major immune cell compartments based on their phenotype (Figure 1*A*–*D*), namely $CD3^-CD7^+$ innate lymphoid cells (ILCs; including natural killer (NK) cells), CD4 T cells, CD8/$\gamma\delta$ T cells, myeloid cells, and B cells. As expected, significantly higher frequencies of $CD3^-CD7^+$ cells were observed in duodenum of RCDII patients in both data sets (Figure 1*E* and *F*). Control duodenal samples showed higher frequencies of CD8/$\gamma\delta$ T cells than RCDII duodenum. CD4, myeloid, and B cells were present to a lesser extent in both control and RCDII duodenum without significant differences. In paired peripheral blood samples, we observed a significant decrease in CD4 T cells and an increase in CD8 T cells (data not shown). For panel 2, which only contains RCDII-derived $CD45^+$ cells, we observed similar percentages in duodenum (Figure 1*D*, *G*, and *H*) and peripheral blood (data not shown) for all major immune lineages when compared with data from panel 1. Thus, the duodenal RCDII samples are characterized by a significant increase in $CD3^-CD7^+$ cells in combination with a significantly lower number of CD8/$\gamma\delta$ T cells, whereas peripheral blood samples showed a significant decrease in CD4 T cells and an increase in CD8 T cells.

Mass Cytometric Analysis of $CD3^-CD7^+$ Cells in Control and RCDII Tissues

For further characterization of the 6 major immune lineages of both data sets in more detail, we analyzed every lineage separately using HSNE and t-distributed stochastic neighborhood embedding (tSNE) in Cytosplore. First, we

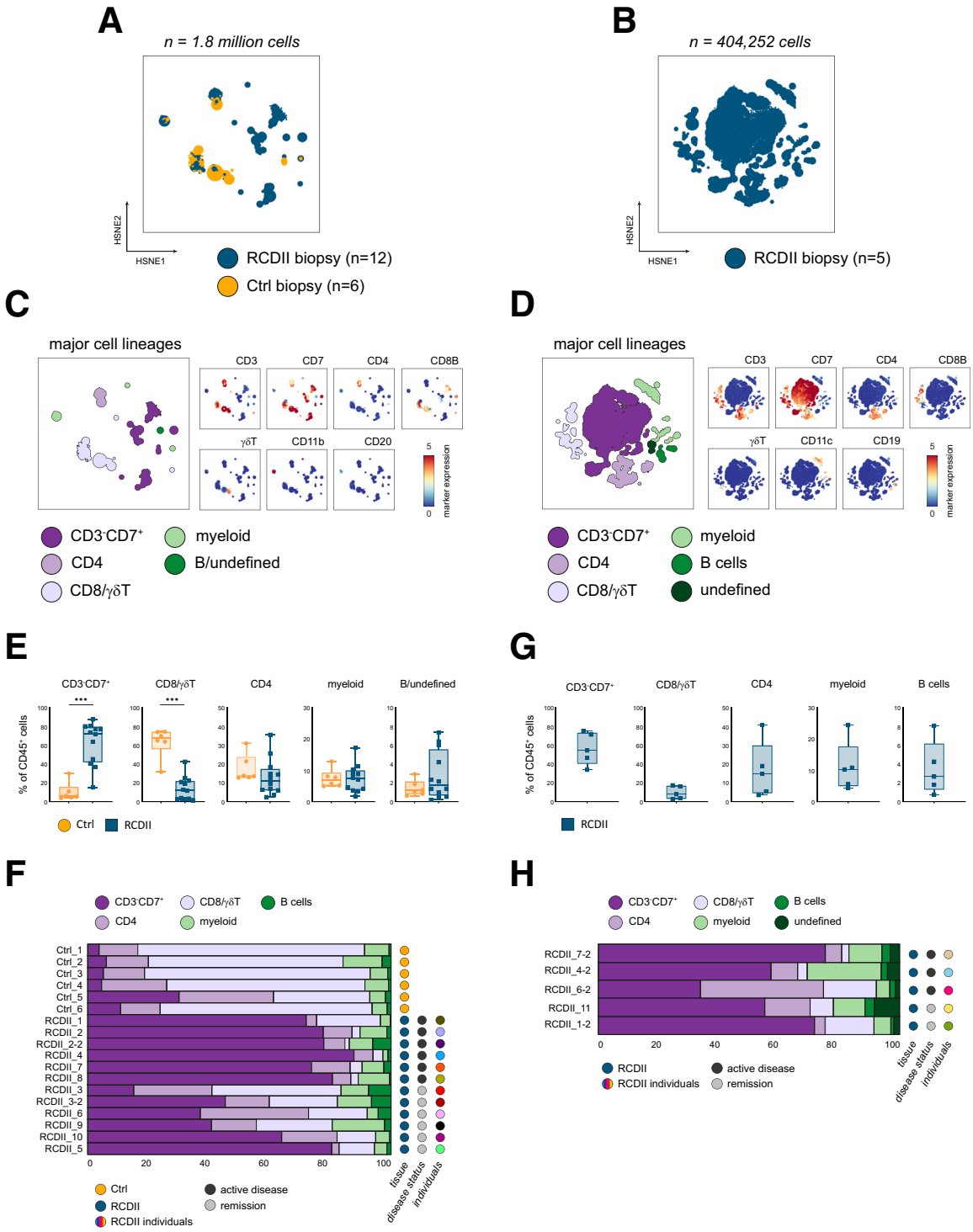

Figure 1. Two mass cytometric data sets of duodenal CD45$^+$ cells. (*A*) HSNE embedding of CyTOF data set 1 showing 1.8 million cells derived from control (n = 6; 52,801 cells) and RCDII biopsy specimens (n = 12; 805,825 cells). (*B*) HSNE embedding of CyTOF data set 2 showing 404,252 cells derived from RCDII biopsy specimens (n = 5). (*C*) HSNE embedding showing identified major immune cell lineages in CyTOF data set 1, including marker expression overlays of HSNE embedding depicted in panel *A*. (*D*) HSNE embedding showing identified major immune cell lineages in CyTOF data set 2, including marker expression overlays of HSNE embedding depicted in panel *B*. (*E*) Frequencies of major lineages among control and RCDII biopsy specimens as the percentage of total CD45$^+$ cells (CyTOF data set 1). (*F*) Lineage frequency outlined per sample biopsy and attributed per tissue, disease status, and RCDII individual (CyTOF data set 1). (*G*) Frequencies of major lineages among RCDII biopsy specimens as the percentage of total CD45$^+$ cells (CyTOF data set 2). (*H*) Lineage frequency outlined per sample biopsy and attributed per tissue, disease status, and RCDII individual (CyTOF data set 2). (*C* and *D*) Colors indicate expression values of arcsine transformed data, ranging from 0 to 5 (blue to red). (*E* and *G*) Significance was calculated using the Mann–Whitney test. ***$P \leq .0001$. Box plots represent the median ± interquartile range. Ctrl, control; RCDII, refractory celiac disease type II.

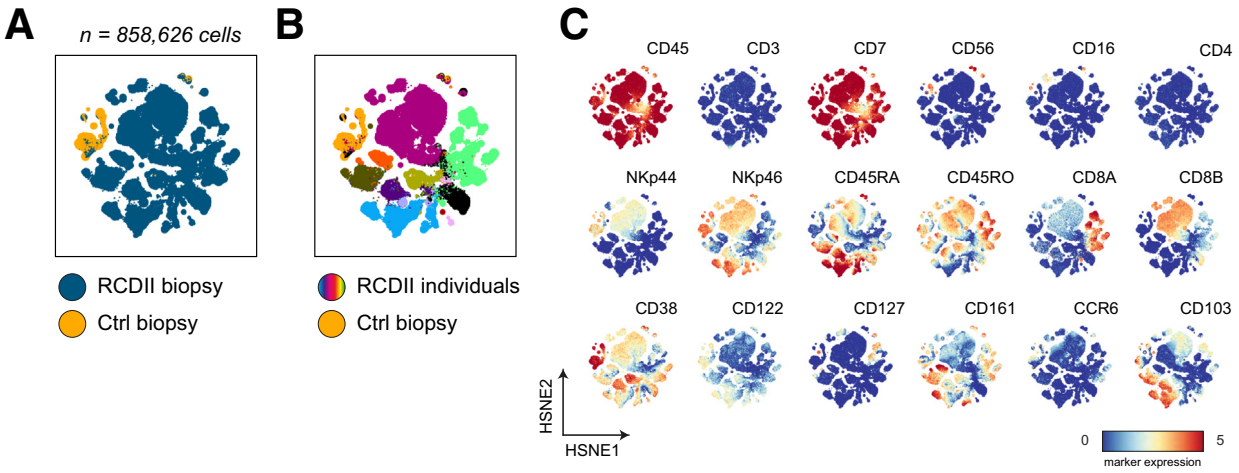
A
n = 858,626 cells
RCDII biopsy
Ctrl biopsy
B
RCDII individuals
Ctrl biopsy
C
CD45
CD3
CD7
CD56
CD16
CD4
NKp44
NKp46
CD45RA
CD45RO
CD8A
CD8B
CD38
CD122
CD127
CD161
CCR6
CD103
HSNE2
HSNE1
0
5
marker expression

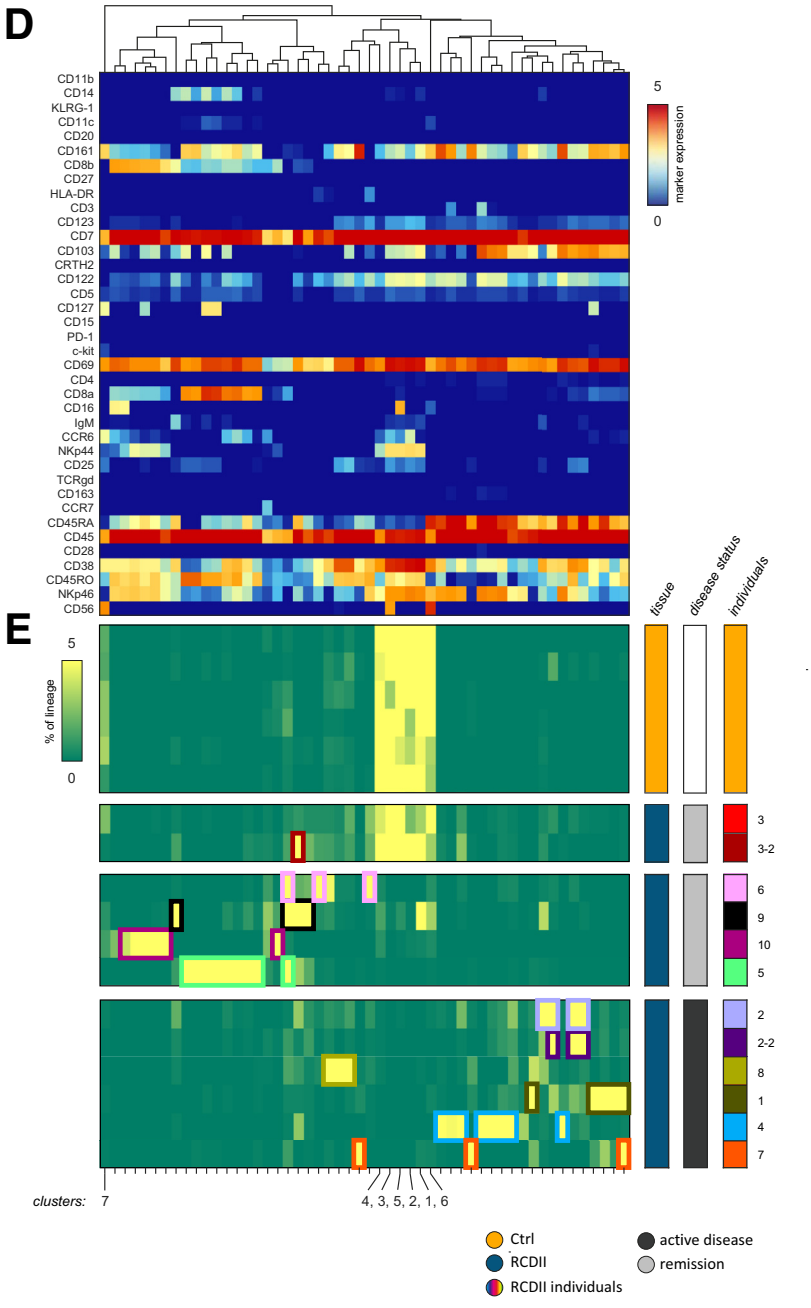
D
CD11b
CD14
KLRG-1
CD11c
CD20
CD161
CD8b
CD27
HLA-DR
CD3
CD123
CD7
CD103
CRTH2
CD122
CD5
CD127
CD15
PD-1
c-kit
CD69
CD4
CD8a
CD16
IgM
CCR6
NKp44
CD25
TCRgd
CD163
CCR7
CD45RA
CD45
CD28
CD38
CD45RO
NKp46
CD56
5
marker expression
0
tissue
disease status
individuals
E
5
% of lineage
0
3
3-2
6
9
10
5
2
2-2
8
1
4
7
clusters:
7
4, 3, 5, 2, 1, 6
Ctrl
RCDII
RCDII individuals
active disease
remission

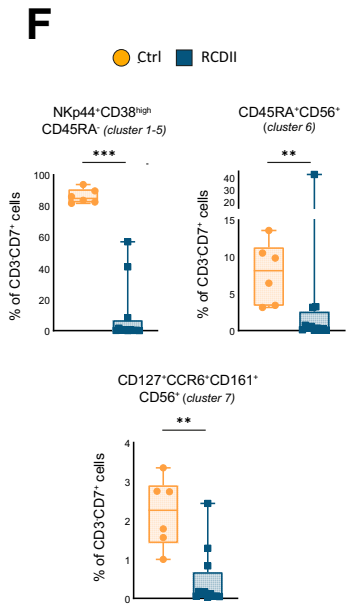
F
Ctrl
RCDII
NKp44+CD38high
CD45RA- (cluster 1-5)
***
% of CD3-CD7+ cells
CD45RA+CD56+
(cluster 6)
**
% of CD3-CD7+ cells
CD127+CCR6+CD161+
CD56+ (cluster 7)
**
% of CD3-CD7+ cells

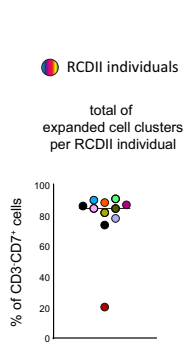
G
RCDII individuals
total of
expanded cell clusters
per RCDII individual
% of CD3-CD7+ cells

focused on the largest compartment in RCDII tissues: the innate $CD3^-CD7^+$ lineage, comprising 72.89% (interquartile range, 41.97–87.78) of $CD45^+$ cells in mass cytometry data set 1 (Figure 1*E*). Within this data set, we performed a 2-level HSNE analysis in Cytosplore on $CD3^-CD7^+$ duodenal cells from control and RCDII patients (n = 858.626 cells in total). At the overview level (Figure 2*A*), the large majority of $CD3^-CD7^+$ cells derived from control biopsy specimens separate from cells from RCDII biopsy specimens. Moreover, cells from each RCDII patient formed a separate cluster, indicative of patient-specific phenotypic features of the aberrant $CD3^-CD7^+$ cells (Figure 2*B*). Figure 2*C* provides an overview of the expression of the immune cell markers analyzed. Phenotype-based hierarchical clustering of all $CD3^-CD7^+$ cells based on these expression profiles resulted in 52 clusters (Figure 2*D*). The associated cell frequency heatmap (Figure 2*E*) visualizes the abundance of these clusters in individual patient samples. The cell frequency heatmap readily identifies a cluster of 6 related immune subsets that are predominant in the biopsy specimens of the controls and largely lacking in the RCD samples (Figure 2*E*, clusters 1–6). Five of these $CD3^-CD7^+$ cell clusters were $NKp44^+NKp46^+CD38^{high}CD45RA^-$ cells (clusters 1–5), and represent the largest population in healthy duodenum (Figure 2*F*). In addition, 4 of these expressed CD103 (clusters 1, 2, 3, and 5), indicating they are derived from the intestinal epithelium, and 1 (cluster 3) was $CD56^+$. Finally, cell cluster 6 contains $CD45RA^+CD56^+$ NK cells (Figure 2*D*–*F*). Notably, these cell populations also were present in RCDII patient 3 (Figure 2*E*, samples 3 and 3-2, in remission), but in hardly any of the other patient samples, including those in remission (Figure 2*E*, samples 5, 6, 9, and 10). In contrast, RCDII duodenal $CD3^-CD7^+$ cells distinguished themselves by expanded cell population(s) with individual-specific marker expression profiles (Figure 2*A*–*E*). This interpatient aberrant cell heterogeneity was caused by differential expression of CD8α, CD8β, NKp44, NKp46, CD45RA, CD45RO, CD122, CD161, CD127, CCR6, and NKp44 (Figure 2*B*–*E*). For example, patient 5 is characterized by the presence of a cluster of $CD45RO^+CD8\alpha^+CD161^+$ cells while patient 10 harbors primarily $CD8\alpha^+CD8\beta^+NKp44^+$ cells. Two RCDII patients that were included twice at different time points (3, 3-2; 2, 2-2) showed similar expression profiles (Figure 2*D* and *E*), suggesting a relatively stable profile once disease was established. In addition, in most patients multiple expanded cell clusters are present that are distinguished by differential expression of 1 or multiple markers, indicative of intrapatient heterogeneity. For example, patient 4 harbors both 2 highly similar cell clusters that are distinguished by the presence or absence of CD103, while the expression of NKp46 is highly variable among expanded cell clusters in several other patients (5, 6, 9, and 10) (Figure 2*D* and *E*). Lastly, compared with the control samples, a distinct down-regulation of CD122, the shared IL2 and IL15-receptor β-chain, was observed in many of the RCDII $CD3^-CD7^+$ cell clusters (Figure 2*A*, *D*, and *E*).

In the second mass cytometric data set, we analyzed the expression of transcription factors (TFs) on $CD3^-CD7^+$ cells from the second cohort of 5 RCDII patients (n = 259,778 cells) (Figure 3). Here, expression of T-bet was observed on the large majority of cells, in line with the expression of this TF in ILC1 and NK-cell receptor–positive ILC3s.[13] Moreover, low levels of GATA Binding Protein 3 (GATA3) were observed while expression of ILC3-specific TF retinoic acid receptor-related orphan receptor gamma T (RORγT) and NK cell TF Eomes was absent on $CD3^-CD7^+CD56^-$ cells.

Together, these data indicate that in the majority of patients the $CD3^-CD7^+$ immune compartment is distinct from that in healthy controls and that substantial interpatient and intrapatient heterogeneity exists. Although the expression of the transcription factors matches ILC1s and NK-cell receptor–positive ILC3s, the lack of expression of CD127 in the majority of patients sets the aberrant cells apart from classic ILCs.

Phenotypic and Frequency Discrepancies Between Peripheral Blood and Duodenal Aberrant Cells

In parallel, we performed phenotypic and frequency analysis of $CD3^-CD7^+CD56^-$ cells in peripheral blood derived from control and RCDII samples. Substantially increased frequencies of $CD3^-CD7^+CD56^-$ cells were observed in 3 of the 9 RCDII samples (Figure 4*A*). A tSNE analysis of peripheral control and RCDII $CD3^-CD7^+CD56^-$ cells (Figure 4*B*) indicated that the large majority of cells were derived from patients RCDII 3, 3-2, and 6 (Figure 4*C*). Marker expression overlays for this tSNE (Figure 4*D*) showed phenotypic heterogeneity both between and within patients. For example, a sizable

Figure 2. (***See previous page***). **Mass cytometric analysis of $CD3^-CD7^+$ cells in the small intestine.** (*A*) HSNE embedding showing 858,626 cells from RCDII biopsy specimens (n = 12; 805,825 cells) and control biopsy specimens (n = 6; 52,801 cells) of CyTOF data set 1. (*B*) HSNE analysis showing embedding of individual RCDII $CD3^-CD7^+$ cells and control $CD3^-CD7^+$ cells. (*C*) Marker expression overlays of HSNE embedding depicted in panels *A* and *B*. Arcsine transformed data resulting in median marker expression values, ranging from 0 to 5 (blue to red). (*D*) Heatmap representing median marker expression values along with hierarchical clustering. (*E*) Cluster frequencies within $CD3^-CD7^+$ cells, frequencies ranging from 0 to 5. Clusters were attributed per tissue, disease status, and RCDII individual. (*F*) Frequencies of specific clusters (clusters 1–5; 6 and 7) among control and RCDII biopsy specimens within $CD3^-CD7^+$ cells. (*G*) Expanded $CD3^-CD7^+$ cell clusters, specific per RCDII individual. A value of $\geq$5% was defined for individual-specific expansion. (*E* and *F*) Significance was calculated using the Mann–Whitney test. $^{**}P \leq .001$, $^{***}P \leq .0001$. Box plots represent the median ± interquartile range. Ctrl, control; RCDII, refractory celiac disease type II.

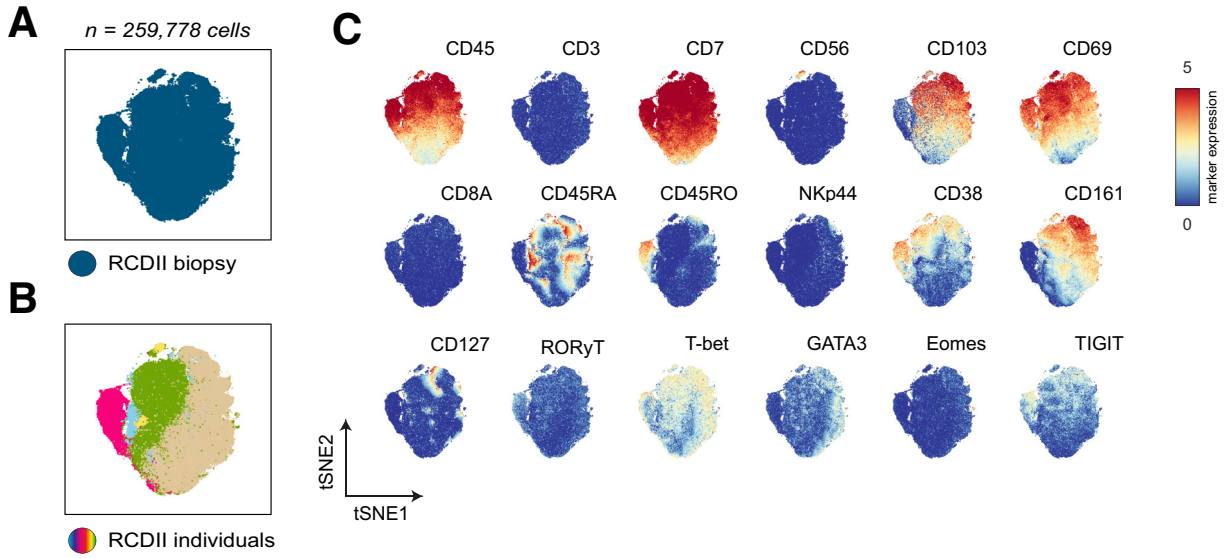

Figure 3. Mass cytometric analysis of CD3$^-$CD7$^+$ cells in the small intestine, CyTOF data set 2. (*A*) tSNE embedding showing 259,778 cells from RCDII biopsy specimens (n = 5), analyzed with CyTOF panel 2. (*B*) tSNE embedding as shown in a visualizing individual embedding of CD3$^-$CD7$^+$ cells derived from 5 RCDII individuals. (*C*) Marker expression overlays of tSNE embedding depicted in panels *A* and *B*. Shown are arcesine transformed data resulting in median marker expression values, ranging from 0 to 5 (blue to red).

proportion of the CD3$^-$CD7$^+$CD56$^-$ cells from sample 3 express CD127, although this marker is not present in samples 3-2 and 6, reflecting interpatient heterogeneity. However, not all CD3$^-$CD7$^+$CD56$^-$ cells from sample 3 express CD127, reflecting intrapatient heterogeneity (Figure 4*C* and *D*). In addition, differential expression of CD161, HLA-DR, CD69, CD38, CD45RA, CD45RO, CD11c, and CD28 contributes to intrapatient heterogeneity (Figure 4*C* and *D*). In general, controls harbored CD16$^+$CD56$^-$ cells and CD25$^+$ ILCs, while NKp46 and dim expression of CD122 was more common in RCDII samples (Figure 4*C* and *D*).

Next, we plotted peripheral blood aberrant cell counts within the CD3$^-$CD7$^+$ lineage against aberrant cell counts of total IELs as determined by diagnostic flow cytometry data (Figure 4*E*). Strikingly, the 3 patients with the highest aberrant cell expansions in PBMCs (individual 3, 3-2, and 6) had the lowest aberrant cell counts in duodenum. In addition, aberrant cell frequencies in peripheral blood did not correlate with disease status in terms of villous atrophy because these 3 individuals were in remission at these time points (Figure 2*D*). To compare immune phenotypes of aberrant cells in duodenum and periphery, we performed a tSNE analysis using CD3$^-$CD7$^+$CD56$^-$ cells derived from paired biopsy and PBMC samples from individual 6 (Figure 4*F*). Here, duodenal CD3$^-$CD7$^+$CD56$^-$ cells showed clear expression of CD69 and CD45RO whereas peripheral cells distinguished themselves by expression of CD103 and CD45RA (Figure 4*G*). Overlapping markers also were observed, such as NKp46 and HLA-DR.

To conclude, we observed phenotypic discrepancy between duodenal and aberrant cell phenotypes. Moreover, peripheral aberrant CD3$^-$CD7$^+$CD56$^-$ cells can be discriminated from control cells by the lack of CD25 and expression of NKp46 and CD122^{dim}. Similar to observations in duodenum, peripheral aberrant cells show interpatient and intrapatient heterogeneity. Finally, a low percentage of duodenal aberrant cells (of total IELs) did not correlate with low aberrant cell counts in peripheral blood, and vice versa.

Two scRNA-Seq Data Sets of Duodenal RCDII CD45$^+$ Cells

For an unbiased, in-depth analysis of duodenal immune cells in RCDII, we performed scRNA-seq on bead-isolated CD45$^+$ IELs and LP cells (see the Methods section), derived from 2 RCDII patients (Table 1), 1 patient who was included in our mass cytometry analysis at the same time point (RCDII 4-2). At the time of inclusion the percentage of aberrant cells, as determined by flow cytometry (not shown), was 50% and 95% of total IELs for patients 12 and 4-2, respectively. In total, we performed sequencing on approximately 3000 cells from patient 1 (RCDII 12) and approximately 5000 cells from patient 2 (RCDII 4-2). scRNA-seq detected a median gene expression of 1164 and 1127 per cell in data set RCDII 12 and RCDII 4-2, respectively. For further gene expression analysis, we used the Seurat pipeline (New York, NY).[14] After performance of quality controls, we generated 2 data sets: data set 1 of 1898 cells with 16,309 genes expressed (RCDII 12); and data set 2 of 4505 cells with 15,503 genes expressed (RCDII 4-2) (see the Methods section). Both data sets were analyzed separately. After quality control and clustering, we used gene expression profiles for identification of cell clusters and annotation.

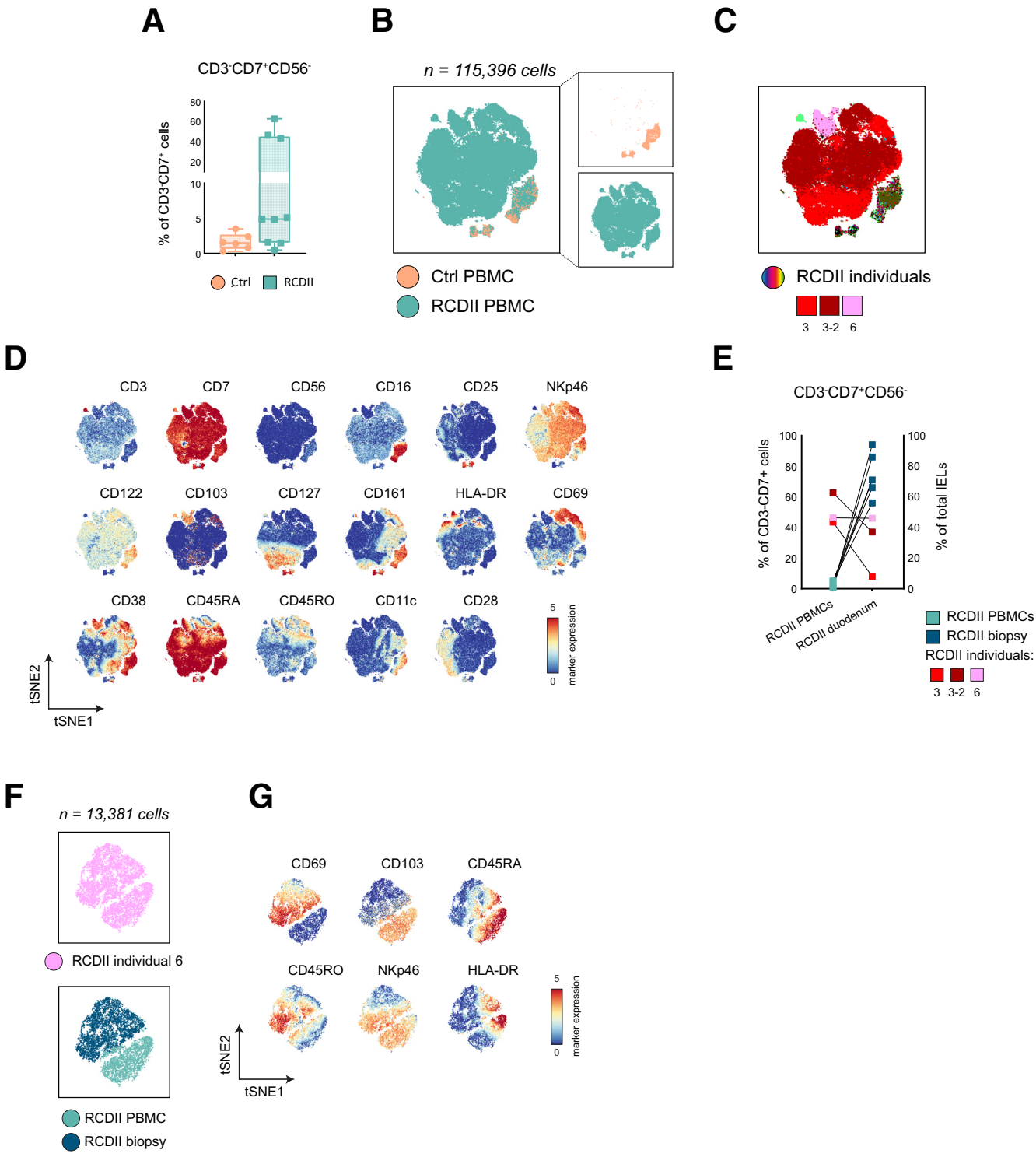

Figure 4. Phenotypic and frequency discrepancies between peripheral blood and duodenal aberrant cells. (*A*) Frequencies of CD3$^-$CD7$^+$CD56$^-$ cells within the CD3$^-$CD7$^+$ cell population derived from PBMCs of controls (n = 6) and RCDII patients (n = 9). (*B*) tSNE embedding showing CD3$^-$CD7$^+$CD56$^-$ cells (n = 115,396) derived from control and RCDII PBMCs. (*C*) tSNE embedding showing CD3$^-$CD7$^+$CD56$^-$ peripheral cells derived from RCDII individuals. One color was attributed per RCDII individual; colors of RCDII tissues 3, 3-2, and 6 are shown. (*D*) Marker expression overlays of tSNE embedding depicted in panels *B* and *C*. (*E*) Frequencies of peripheral blood CD3$^-$CD7$^+$CD56$^-$ cells within the CD3$^-$CD7$^+$ cell population derived from RCDII patients vs duodenal CD3$^-$CD7$^+$CD56$^-$ cells as the percentage of total IELs, as determined by flow cytometry. (*F*) tSNE embedding showing CD3$^-$CD7$^+$CD56$^-$ cells (n = 13,381) derived from RCDII individual 6, derived from PBMCs and duodenal RCDII tissue. (*G*) Marker expression overlays of tSNE embedding depicted in panel *F*. (*D* and *G*) Arcsine transformed data resulting in median marker expression values, ranging from 0 to 5. (*A*) Significance was calculated using the Mann–Whitney test. Box plots represent the median ± interquartile range. Ctrl, control. RCDII, refractory celiac disease type II.

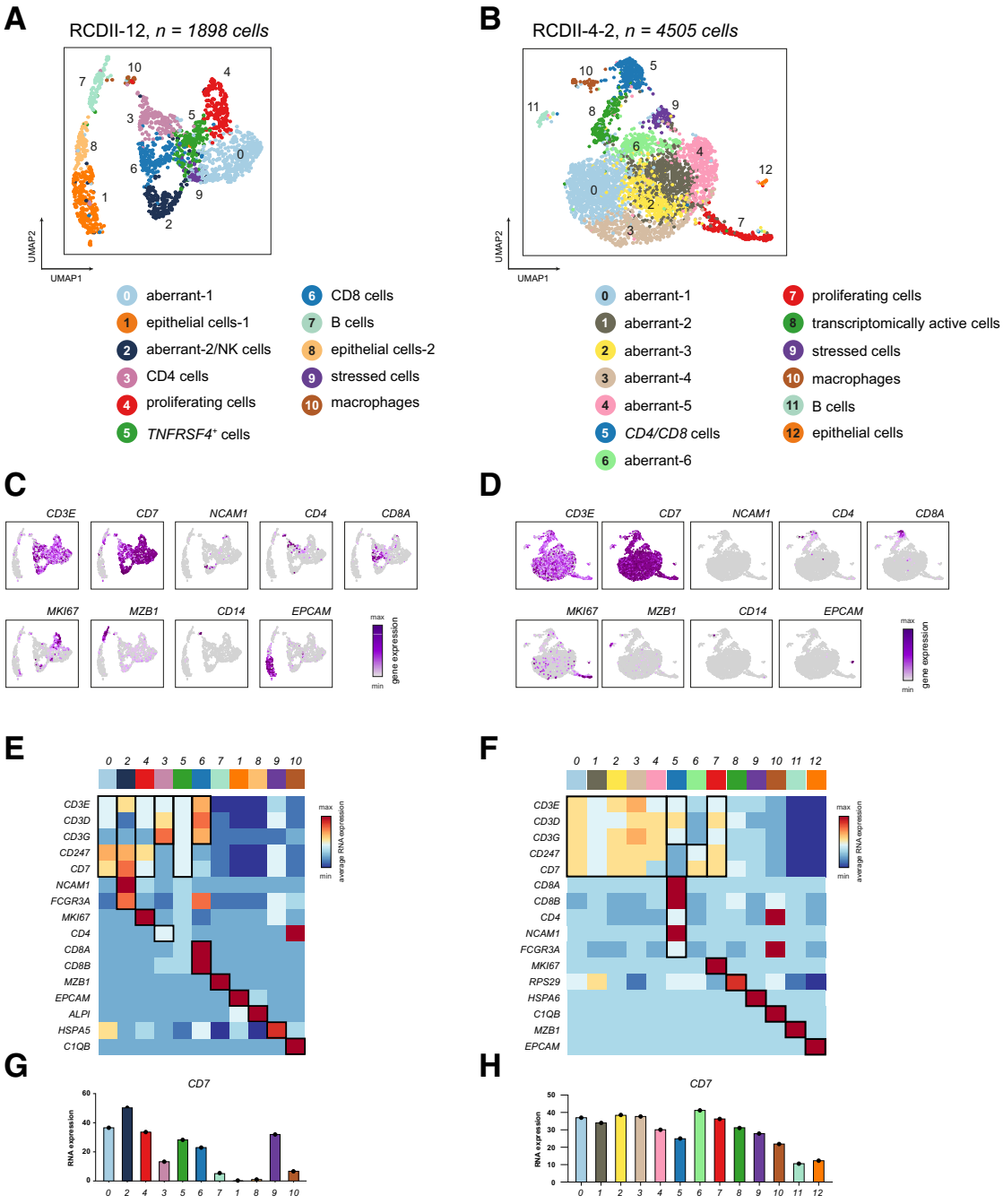

Figure 5. Two scRNA-seq data sets of RCDII duodenal CD45$^+$ cells. (*A*) UMAP embedding showing 1898 duodenal CD45$^+$ single cells derived from patient RCDII 12. Clustering resulted in 11 cell clusters, aberrant-1 (cluster 0; n = 437), epithelial cells-1 (cluster 1; n = 243), aberrant-2/NK cells (cluster 2; n = 206), CD4 cells (cluster 3; n = 199), proliferating cells (cluster 4; n = 194), *TNFRSF4*$^+$ cells (cluster 5; n = 183), CD8 cells (cluster 6; n = 181), B cells (cluster 7; n = 90), epithelial cells-2 (cluster 8; n = 89), stressed cells (cluster 9; n = 51), and macrophages (cluster 10; n = 25 cells). Colors and numbers indicate distinct cell clusters. (*B*) UMAP embedding showing 4505 duodenal CD45$^+$ single cells derived from patient RCDII 4-2. Clustering resulted in 13 cell clusters, aberrant-1 (cluster 0; n = 1164), aberrant-2 (cluster 1; n = 655), aberrant-3 (cluster 2; n = 524), aberrant-4 (cluster 3; n = 494), aberrant-5 (cluster 4; n = 460), *CD4/CD8* cells (cluster 5; n = 283), aberrant-6 (cluster 6; n = 275), proliferating cells (cluster 7; n = 242), transcriptomically active cells (cluster 8; n = 185), stressed cells (cluster 9; n = 97), macrophages (cluster 10; n = 56), B cells (cluster 11; n = 44), and epithelial cells (cluster 12; n = 26). (*C* and *D*) Feature plots showing normalized single-cell gene expression data of immune lineage genes as expression overlays for UMAP embeddings depicted in panels *A* and *B*. Color bar from grey (minimum [min]) to purple (maximum [max]). (*E* and *F*) Heatmap showing average RNA expression per cluster of immune lineage genes. Color bar from blue (min) to red (max). Colors and cell cluster numbers as indicated in panels *A* and *B*, respectively. (*G* and *H*) CD7 average gene expression per cluster depicted in bar plots. Expression data correlate with CD7 expression as shown in panels *E* and *F*, respectively. Colors and cell clusters are numbered as indicated in panels *A*, *B*, *E*, and *F*.

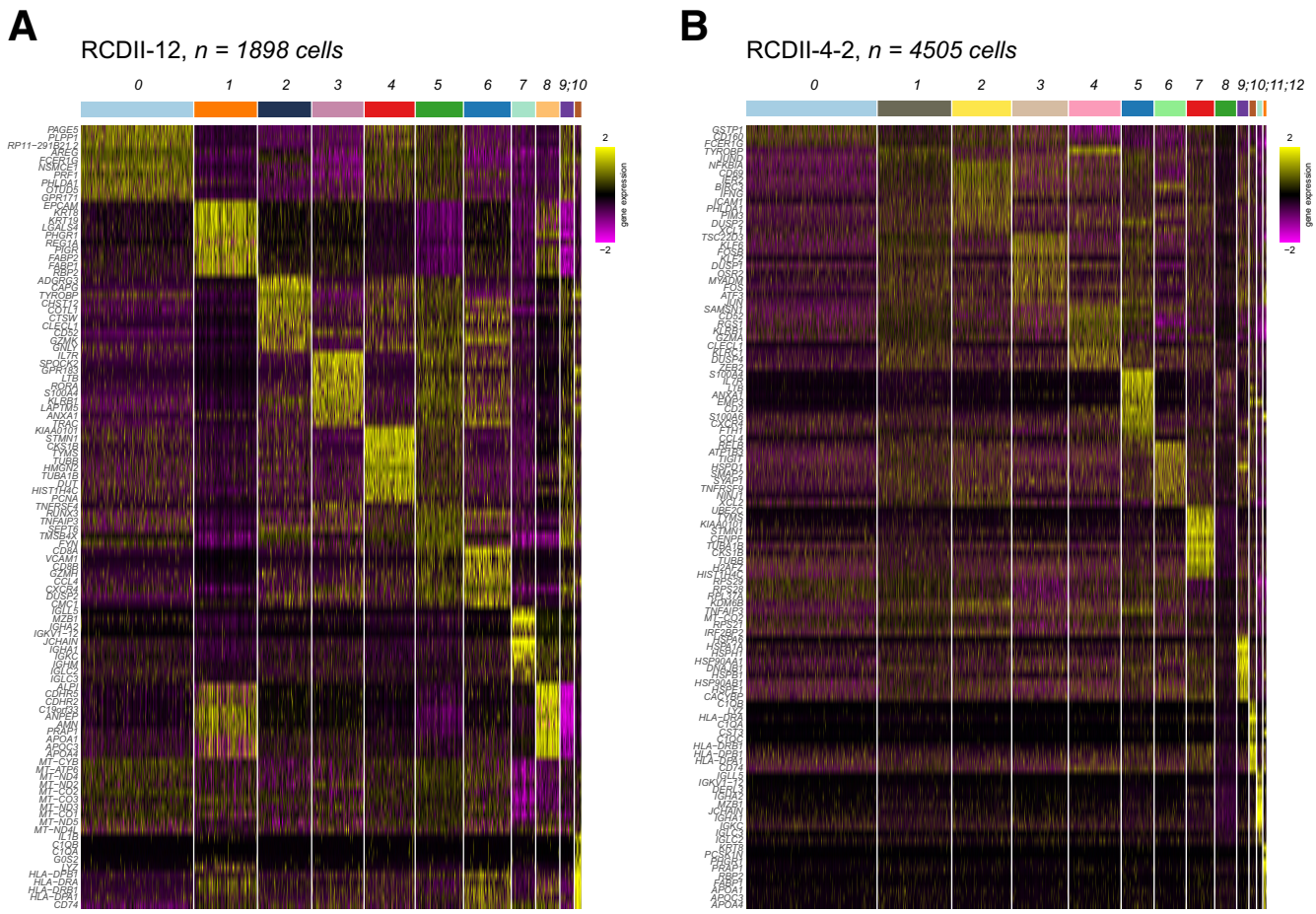

Figure 6. Top 10 differentially expressed genes in two data sets of duodenal RCDII CD45$^+$ cells. (*A*) Heatmap showing the top 10 DE genes from 11 identified cell clusters as visualized in UMAP embedding of 1898 cells from RCDII 12, shown in Figure 5*A*. Colors and numbers indicate different cell clusters. (*B*) Heatmap showing the top 10 DE genes of 13 identified cell clusters as visualized in UMAP embedding of 4505 cells from RCDII 4-2, shown in Figure 5*B*. (*A* and *B*) The data visualized are normalized dispersions of single-cell gene expression data (z-score, color bare from purple to yellow). Colors and cell clusters are numbered as indicated in Figure 5*A* and *B*.

Clustering of data set RCDII 12 showed 12 clusters. Highly similar gene expression profiles were observed for 2 clusters that therefore were merged (data not shown), resulting in 11 distinct clusters for RCDII 12 (Figure 5*A*). For data set RCDII 4-2, unbiased uniform manifold approximation and projection (UMAP) clustering resulted in 13 cell clusters (Figure 5*B*). For cell annotation in both data sets, the top 10 differentially expressed (DE) gene expression profiles identified some, but not all, cell clusters (Figure 6*A* and *B*). For correct annotation of these as yet unidentified cells, we visualized major lineage gene expression plots (Figure 5*C* and *D*) and the average RNA expression of lineage genes per cluster (Figure 5*E* and *F*). In both data sets, aberrant cell clusters were identified based on relatively high *CD7* expression, varying amounts of T-cell receptor (TCR)-CD3 complex chains (*CD3E*, *CD3D*, *CD3G*, and *CD247ζ*), and the absence of *NCAM1* (CD56), *CD4*, *CD8A*, and *CD8B* expression (RCDII 12, cluster 0; RCDII 4-2, cluster 0-4, 6) (Figures 5*A–F* and 6*A* and *B*). In data set RCDII 12, we observed partial expression of *NCAM1* in cell cluster 2 (Figure 5*C*), which therefore was annotated as aberrant-2/NK cells. Furthermore, in data set RCDII 12 we identified *CD4* and *CD8* cells showing lower average *CD7* expression (cluster 3, 6) (Figure 5*C* and *E*) and a cluster of *TNFRSF4*$^+$ (OX40) cells with a dim average expression of *CD3* genes and *CD7* (cluster 5) (Figures 5*E* and 6*A*). Cluster 5 shows overlap in DE genes with all other aberrant/T lymphocyte clusters in this data set (Figure 6*C*), suggesting these cells are differentiating. In data set RCDII 4-2, we identified a *CD4/CD8* cell cluster (cluster 5) (Figure 5*D* and *F*) and a transcriptomically active cell cluster as indicated by *RPS29* (cluster 8) (Figure 5*D* and *F*). In addition, in both data sets, we identified B cells (*MZB1*, marginal zone B1), macrophages (*C1QB*, complement C1q subunit), epithelial cells (*EPCAM*, *ALPI* [intestinal alkaline phosphatase]), stressed cells (*HSP* genes), and proliferating cells (*MKI67*) (Figure 5*C-F*). In both data sets, these proliferating cell clusters (RCDII 12 cluster 4; RCDII 4-2, cluster 7) showed high levels of average *CD7* RNA expression (Figure 5*G* and *H*), suggesting these clusters harbor proliferating aberrant cells.

Analysis of Duodenal CD3$^-$CD7$^+$ Cells Within the Two scRNA-Seq Data Sets

To analyze the aberrant cell population at higher resolution, we computationally isolated aberrant/NK cell clusters from both data sets. From RCDII 12, we isolated clusters 0 and 2, containing 643 cells; and from RCDII 4-2, we isolated clusters 0–4 and 6, containing 3573 cells.

First, we analyzed data set RCDII 12. Unbiased reclustering of the cells yielded 6 clusters (Figure 7*A*). *CD3E*, *CD7*, *KLRF1* (NKp80), and *FCGR3A* gene expression overlays were plotted (Figure 7*B*) and the top 12 DE genes were shown (Figure 7*C*). Here, cluster 5 contains *PIGR*$^+$ (poly-Ig receptor) epithelial cells. In Figure 7*C*, expression profiles of the remaining 5 cell clusters showed similarity between clusters 0, 1, and 2, and between clusters 3 and 4. Upon further analysis of DE gene expression profiles, we observed that aberrant cell clusters 0, 1, and 2 showed expression of *CD69*, immune checkpoint molecules *TIGIT* and *TNFRSF9* (CD137), and T-cell–associated genes *CD2*, *CD3D*, *CD44*, and *IL10*. However, next to shared genes, these aberrant cell clusters also showed significant differences in their gene expression profiles. Likewise, clusters 3 and 4 share similar expression of genes, such as *GZMK* and *GNLY*, both linked to cytolytic potential, but also show significant differences in their gene expression profile.

Finally, we scrutinized the scRNA-seq data for corresponding mass cytometric markers and plotted the RNA expression data for these markers (Figure 7*D*). With the exception of TIM-3 (*HAVCR2*), which was not observed on CD3$^-$CD7$^+$ cells at the protein level, the widespread expression of *CD7*, *ITGAE* (CD103), *KLRB1* (CD161), *IL2RB*, and *TIGIT* corresponded to the mass cytometry data. However, expression of *FCGR3A*, *IL2RA* (CD25), *CD38*, *EOMES*, and *GATA3* was found in only part of the aberrant cell clusters, indicative of heterogeneity in the aberrant cell population of this patient. Finally, in a functional analysis we observed substantial expression of *CD74* in all 5 aberrant cell clusters, while both *CD74*, *HLA-DRB1*, and *HLA-DRA1* were expressed by the epithelial cell cluster, indicative of antigen presentation via HLA-class II (Figure 7*E*). Examination for cytokines showed high *GZMB/PRF1* expression in all 5 aberrant/NK cell clusters, whereas few cells showed *IFNG* expression.

A similar analysis approach was performed for data set RCDII 4-2, containing 3572 cells, resulting in 8 distinct cell clusters indicative of intrapatient heterogeneity in the aberrant cell population (Figure 8*A*) (2 clusters merged based on similar gene expression profiles). Gene expression overlays were negative for *KLRF1* and *FCGR3A*, indicating this data set did not contain NK cells (Figure 8*B*). Along with the top 12 DE gene profiles (Figure 8*C*), we identified 6 aberrant cell clusters, *IL7R*$^+$ cells, and a transcriptomically active cell cluster (Figure 8*A*–*C*). Similar to RCDII 12, we observed expression of *CD69*, *ITGAE*, *TIGIT*, *TNFRSF9*, *GZMA*, *GZMB*, *IFNG*, *KLRB1*, *KLRC1* (NKG2A), and *CD74* (Figure 8*C*–*E*). Finally, we observed *TUBA1A* expression, indicative of cell proliferation, in several aberrant cell clusters. Compared with RCDII 4-2, aberrant cell clusters in this analysis showed high *IFNG* expression in most aberrant cell clusters, whereas fewer cell clusters showed *GZMB* expression (Figure 8*E*).

Taken together, these results show significant differences in the gene expression profiles both between and within the aberrant cell population in 2 RCDII patients, confirming interpatient and intrapatient aberrant cell heterogeneity.

RCDII iCD3$^+$sCD3$^-$CD7$^+$ Cells Display Proliferation, Interpatient Heterogeneity, and Co-localization With CD163$^+$ antigen-presenting cells (APCs) In Situ

To examine the spatial distribution of innate and adaptive immune cells in RCDII duodenum in situ, we performed imaging mass cytometry using an antibody panel containing 40 antibodies (see the Methods section), specifically developed for the analysis of snap-frozen duodenal tissue. We applied this panel to tissue sections of 1 control and 2 newly diagnosed RCDII patients who also were included for the generation of the single mass cytometry data set (Ctrl-3, RCDII 2, RCDII 8, same time points). A spectral color, pixel-based analysis was used for data visualization (see the Methods section).

First, we visualized structural markers and lineage markers in sample RCDII 8 (Figure 9*A*). Here, vimentin and E-cadherin identify the lamina propria and epithelium, respectively. In further images, E-cadherin was shown for orientation. Moreover, we visualized smooth muscle actin (SMA) identifying the muscularis mucosae, arterioles and venules, neural networks (CD56), lymphatics (D2-40), and capillaries (CD34, CD141). CD45$^+$ immune cells were abundant in both the epithelial layer and LP. In the middle and lower parts of the villi, we observed CD138$^+$ plasma B cells (Figure 9*A*) and heterogeneous expression of CD19 and CD27 (data not shown). Myeloid cells, specifically CD68$^+$CD163$^+$ M2 macrophages, were more prominent just below the epithelial layer and toward the top of the villi; while lower in the LP these cells were scattered. Similarly, CD11c$^+$ DCs were scattered throughout the LP.

In general, aberrant cells are characterized by iCD3 expression in combination with cell surface CD7 and lack of CD4 and CD8. We therefore classified CD3$^+$CD7$^+$CD4$^-$CD8$^-$ cells as aberrant cells in these tissue sections. Analysis showed aberrant cells were in abundance throughout the epithelial layer while CD4/CD8 T cells were located primarily in the lamina propria. In addition, aberrant cells also were present in the lamina propria (Figure 9*B*, regions 1 and 2), indicating migration from the epithelial layer into the LP. This is in line with our single-cell mass cytometry data showing the lack of CD103 expression by certain aberrant cell populations. Strikingly, in the LP, these aberrant cells co-localized with CD163$^+$ APCs (M2 macrophages) (Figure 9*B*, region 1), which may indicate functional interaction between these 2 cell types. Moreover, in a subset of intraepithelial aberrant CD7$^+$ cells we detected expression of Ki-67, indicative of cell proliferation (Figure 9*C*). Finally, the analysis showed that aberrant CD7$^+$ cells in patient

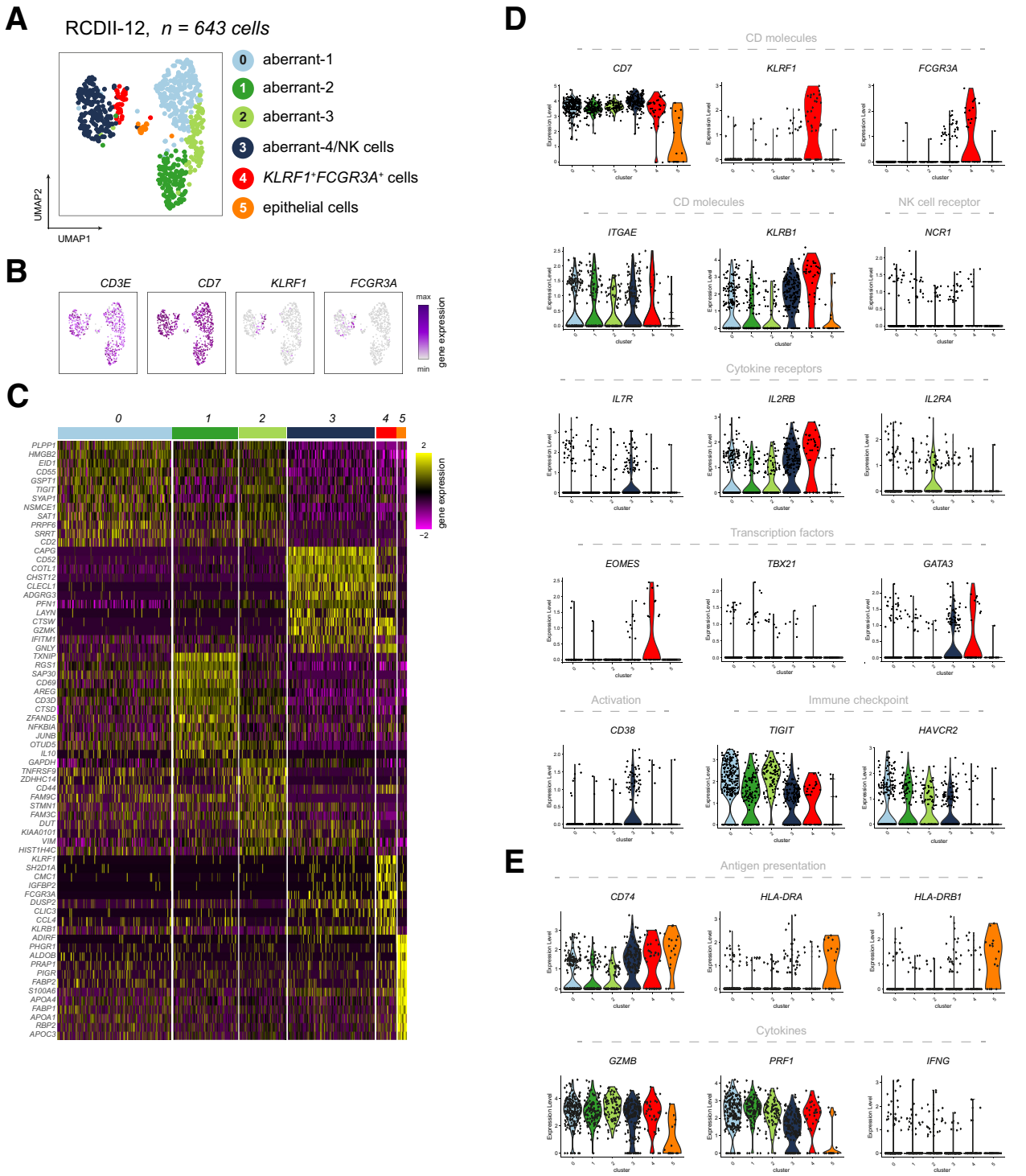

Figure 7. scRNA-seq analysis of duodenal aberrant/NK cells from RCDII 12. (*A*) UMAP embedding showing 643 duodenal $CD3^{-}CD7^{+}$ cells of scRNA-seq data set RCDII 12. Clustering resulted in 6 distinct cell clusters, aberrant-1 (cluster 0; n = 214 cells), aberrant-2 (cluster 1; n = 165 cells), aberrant-3 (cluster 2; n = 122 cells), aberrant-4/NK cells (cluster 3; n = 88 cells), $KLRF1^{+}FCGR3A^{+}$ cells (cluster 4; n = 37 cells), and epithelial cells (cluster 5; n = 17 cells). Colors and numbers indicate distinct cell clusters. (*B*) Feature plots showing log-normalized single-cell gene expression of *CD3E*, *CD7*, *KLRF1*, and *FCGR3A*. Color bar from grey (minimum [min]) to purple (maximum [max]). (*C*) Heatmap showing the top 12 DE genes in each cluster as normalized dispersions of single-cell gene expression data (z-score, color bar from purple to yellow). Colors and numbers are as indicated in panel *A*. (*D*) Violin plots showing log-normalized gene expression data per cluster of selected genes correlating to markers used in the mass cytometric antibody panels. Cluster colors and numbers are indicated in panel *A*. (*E*) Violin plots showing log-normalized gene expression data per cluster of selected genes correlating to functionality. Cluster colors and numbers are indicated in panel *A*.

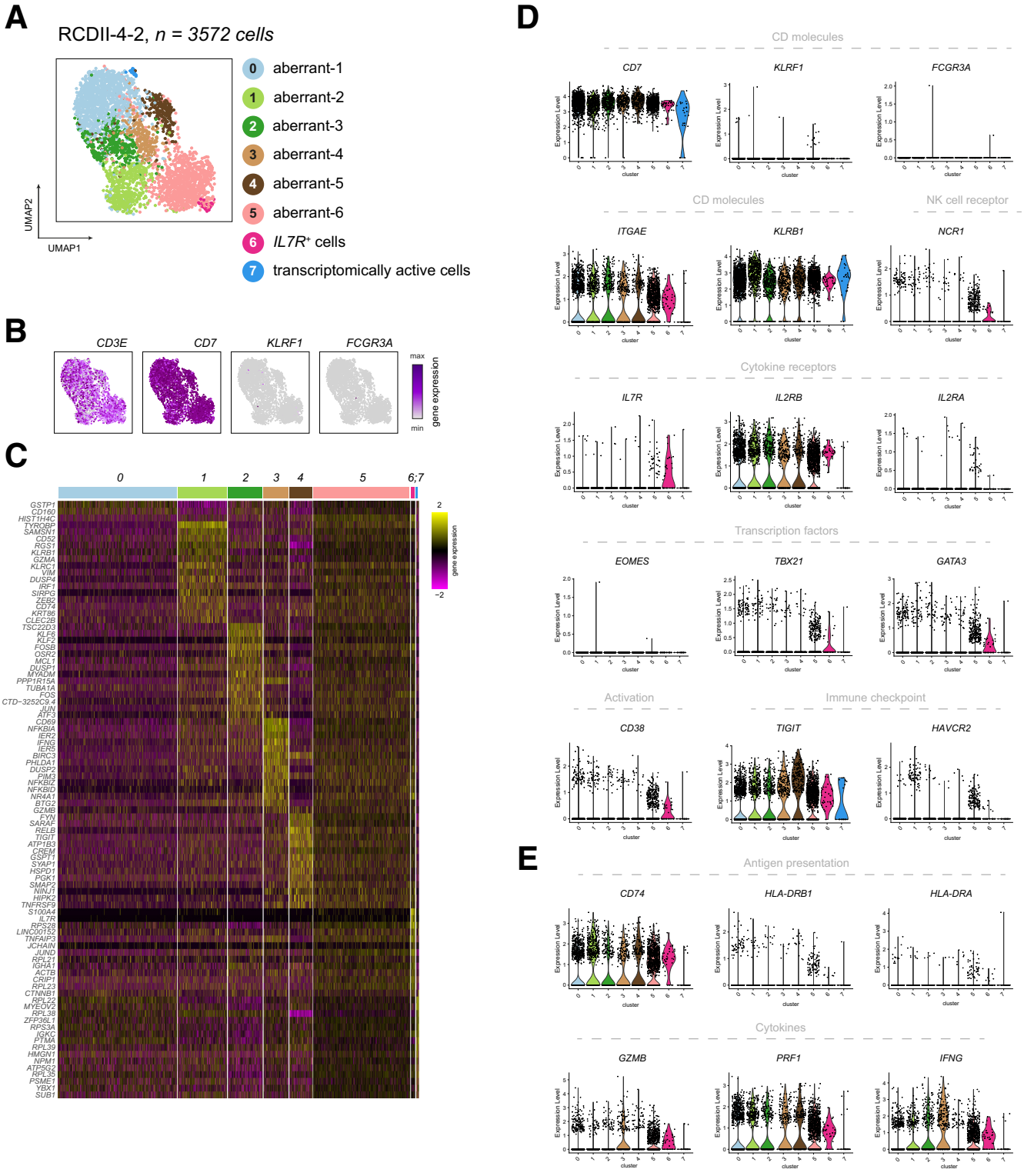

Figure 8. scRNA-seq analysis of duodenal aberrant/NK cells from RCDII 4-2. (*A*) UMAP embedding showing 3572 duodenal CD3$^-$CD7$^+$ cells of scRNA-seq data set RCDII 4-2. Clusters resulted in 8 distinct clusters, aberrant-1 (cluster 0; n = 1203 cells), aberrant-2 (cluster 2; n = 498 cells), aberrant-3 (cluster 3; n = 351 cells), aberrant-4 (cluster 4; n = 251 cells), aberrant-5 (cluster 5; n = 235 cells), aberrant-6 (cluster 5; n = 975 cells), *IL7R*$^+$ cells (clusters 6; n = 36 cells), and transcriptomically active cells (cluster 7; n = 23 cells). Colors and numbers indicate distinct cell clusters. (*B*) Feature plots showing log-normalized single-cell gene expression of *CD3E*, *CD7*, *KLRF1*, and *FCGR3A*. Color bar from grey (minimum [min]) to purple (maximum [max]). (*C*) Heatmap showing the top 12 DE genes in each cluster as normalized dispersions of single-cell gene expression data (z-score, color bar from purple to yellow). Colors and numbers are indicated in panel *A*. (*D*) Violin plots showing log-normalized gene expression data per cluster of selected genes correlating to markers used in the mass cytometric antibody panels. Cluster colors and numbers are indicated in panel *A*. (*E*) Violin plots showing log-normalized gene expression data per cluster of selected genes correlating to functionality. Cluster colors and numbers as indicated in panel *A*.

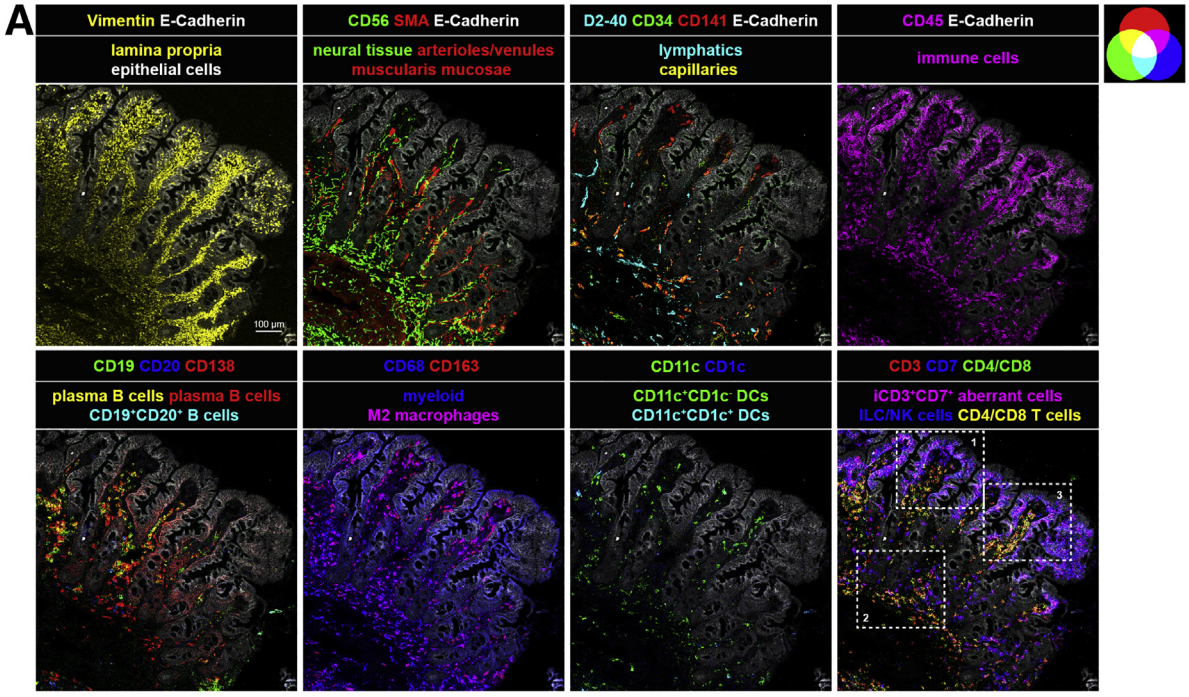

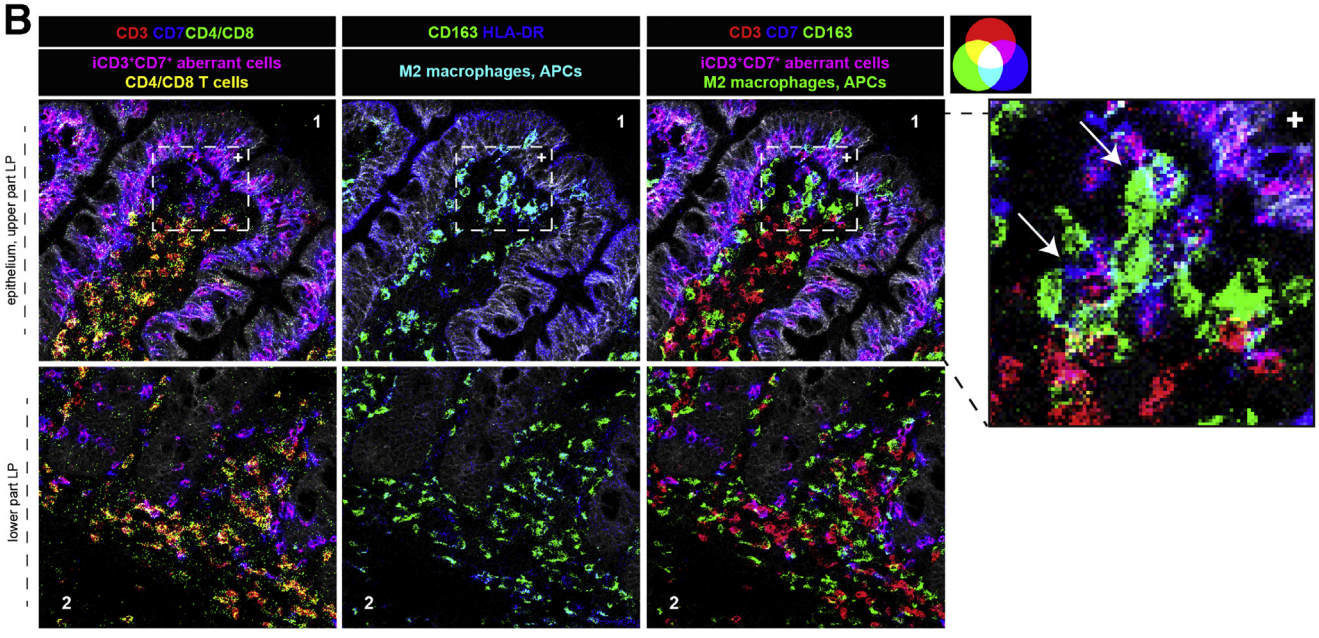

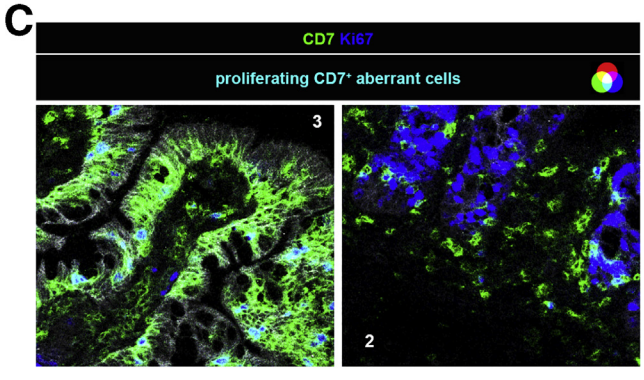

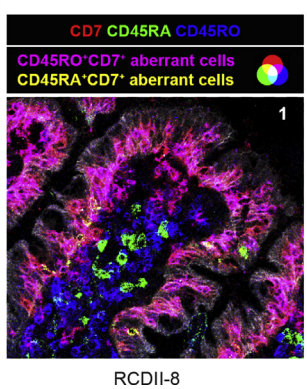

RCDII-8

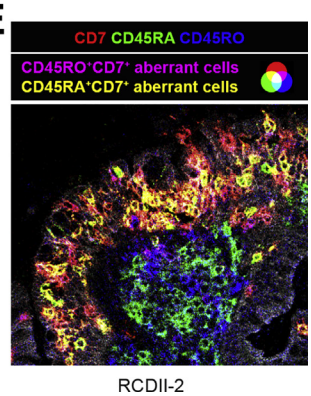

RCDII-2

RCDII 8 were exclusively CD45RO$^+$CD7$^+$ (Figure 9*D*), while both CD45RO$^+$CD7$^+$ or CD45RA$^+$CD7$^+$ were present in patient RCDII 2 (Figure 9*E*). In conclusion, the imaging mass cytometry confirms the interpatient heterogeneity observed in our single-cell mass cytometry data, shows that proliferating aberrant cells are present in these 2 newly diagnosed RCDII patients, and shows co-localization of aberrant cells with CD68$^+$CD163$^+$ APCs.

Discussion

In this study, we performed an in-depth analysis of freshly isolated immune cells from RCDII patients by using single-cell mass cytometry and scRNA-seq. Moreover, we developed and used a 40-marker antibody panel for imaging mass cytometric analysis of duodenal tissue sections to visualize the aberrant cells in tissue context. The single-cell mass cytometry analysis showed substantial interindividual and intra-individual heterogeneity of the duodenal aberrant cell population, findings that were corroborated by scRNA-seq analysis of duodenal immune cells. The latter analysis also provided evidence for the presence of proliferating aberrant cells. Imaging mass cytometry data confirmed interpatient heterogeneity and the presence of Ki-67$^+$ intraepithelial aberrant cells in duodenal tissue samples from RCDII patients. In addition, aberrant cells were found to co-localize with CD163$^+$ APCs just underneath the epithelium, potentially pointing to a functional interaction between these CD163$^+$ APCs and aberrant cells. Finally, a comparative analysis of paired duodenal and peripheral blood aberrant cell expansions showed phenotypic differences, suggesting aberrant cell evolution upon migration from the duodenal tissue.

It is of note that a comparison of the single-cell data and imaging mass cytometry results indicated that substantial numbers of both myeloid and B cells go unnoticed in duodenal single-cell suspensions, most likely owing to selective loss during the tissue digestion protocol. This shows the necessity of in situ analysis for complete visualization of duodenal disease pathology in the tissue context. Together, our observations are highly relevant for future research, to improve diagnostics, and develop effective patient-specific therapeutic approaches.

Previous studies have identified Lin$^-$CD7$^+$CD127$^-$CD34^{-5} and atypical NKp44$^+$NKp46$^+$CD103$^+$ innate T-IELs,[5] both present in healthy duodenum, as potential precursors for the aberrant cells in RCDII. The current study identified additional surface markers for discrimination, namely CD38^{high} expression and absence of CD45RA. However, variable expression of several other cell surface markers underlies the observed interpatient and intrapatient heterogeneity within the aberrant cell population. Because it now is well established that a selective growth advantage occurs as a result of gain-of-function mutations within the Janus kinase (JAK)/signal transducer and activator of transcription pathway *(JAK1/STAT3)*,[5,8,9] it is likely that intertumoral and intratumoral heterogeneity may reflect diversity in the outgrowth of Lin$^-$CD7$^+$CD127$^-$CD34$^-$NKp44$^+$ progenitors, in combination with an accumulation of a diverse array of genetic alterations during tumor evolution. It is likely that the outgrowth of aggressive subclones leads to progression of RCDII to EATL. In addition, the observed intertumoral and intratumoral heterogeneity within the RCDII population may underlie variability in response to treatment and severity of disease status. For example, variability in the severity of disease status may be explained by fluctuations in granzyme B/perforin and/or interferon-γ production by aberrant cells,[9,15,16] resulting in epithelial cell damage with sustained villous atrophy.

From a clinical point of view, intertumoral and intratumoral heterogeneity poses a therapeutic challenge that requires personalized therapy including in-depth diagnostics, such as mutation analysis for JAK1 in RCDII to assess for therapeutic efficacy of JAK inhibitors. Moreover, evolving intratumoral heterogeneity demands dynamic, adaptive therapy for stabilization of the tumor population and prevention of detrimental progression.

Interestingly, duodenal imaging data showed co-localization of CD163$^+$ APCs with aberrant cells in the lamina propria just below the epithelium, likely representing migration from the epithelium into the LP. In general, CD163$^+$ tissue macrophages can play a role in wound healing and tissue repair, and are considered anti-inflammatory. As such, they could play a dual role: containment of epithelial damage but simultaneously sustaining an immunosuppressive environment that favors tumor progression. Moreover, they may contribute to therapeutic resistance of cancer cells by expression of IL6, which enhances the JAK/signal transducer and activator of transcription 3 *(JAK1/STAT3)* pathway in tumor cells.[17] The clarification of the role of myeloid cells in RCDII thus deserves further research.

Although the growth of the aberrant cell population has been attributed to survival via IL15-induced anti-apoptotic pathways,[6] contrasting results have been reported with regard to aberrant IEL proliferation. Mention et al[16] noted

Figure 9. (*See previous page*). RCDII iCD3$^+$sCD3$^-$CD7$^+$ cells display interpatient heterogeneity, proliferation, and co-localization with CD163$^+$ APCs in situ. (*A*) Mass cytometry images showing indicated structural and immune lineage markers of 1 representative ROI from sample RCDII 8 in a spectral color–based analysis. *Dashed line squares* (including numbers) depict 3 regions that are visualized further in panels *B–E*. (*B*) Representative mass cytometry images of region 1 (epithelium, upper part of LP) and region 2 (lower part of LP) from sample RCDII 8 showing expression of the indicated immune cell markers. *Dashed line square* within region 1 depicts an enlarged region shown at the right. *Arrows* indicate iCD3$^+$CD7$^+$ cells surrounded by CD163$^+$ APCs. (*C*) Representative mass cytometry images of region 3 (epithelium, upper part of LP) and region 2 (lower part of LP) from sample RCDII 8 showing overlays of CD7 (green) and Ki-67 (blue) expression. (*D*) Representative mass cytometry image of region 1 (epithelium, upper part of LP) from sample RCDII 8 showing overlays of CD7 (red), CD45RA (green), and CD45RO (blue) expression. (*E*) Representative mass cytometry image of epithelium and upper part of LP from sample RCDII 2, showing overlays of CD7 (red), CD45RA (green), and CD45RO (blue) expression.

that aberrant cells did not express Ki-67, while another study observed negative staining for Ki-67 in IL15 transgenic mice despite accumulation of IELs in their duodenum.[6] In contrast, our scRNA-seq and imaging mass cytometry data provide strong evidence for Ki-67 expression and are more consistent with another study showing Ki-67$^+$ expression by 8.8% of aberrant IELs.[15] More specifically, in the scRNA-seq data, we observed that a subset of aberrant IELs express Ki-67 and show a gene expression profile consistent with cell proliferation. Moreover, the CD4 T-cell cytokines tumor necrosis factor-α (TNF-α), IL2, and IL21 were shown to synergize and induce proliferation of aberrant cells.[18] Thus, although previously the IL15-induced anti-apoptotic effect was proposed to result in aberrant cell accumulation,[6] our data suggest that cell proliferation contributes to sustainment and growth of the aberrant cell population as well.

Next to a duodenal immune cell analysis, we observed clonal aberrant cell populations in 2 of 8 (25%) individual RCDII peripheral blood samples; similar numbers were shown in a previous study in 4 of 12 (33%) RCDII patients.[19] However, we observed a mismatch between duodenal and peripheral blood aberrant cell counts: 3 patients with the lowest aberrant cell frequencies in the duodenum showed the highest frequencies in peripheral blood. Thus, blood samples do not accurately predict duodenal aberrant cell counts, and vice versa.

Typically, peripheral CD8 T cells decrease with age and are considered a consistent immune aging marker.[20,21] However, we observed a decrease in the frequency of CD4 T cells in the periphery, coinciding with an increase in CD8 T cells, regardless of disease status. For RCDII, it is plausible that tumor neoantigens will be presented by major histocompatibility complex class I because neoantigens are generated in tumors with a high mutational burden. Therefore, in future studies, we will investigate if the pool of peripheral CD8 T cells in RCDII patients harbor tumor-reactive T cells. Alternatively, the increase in CD8 T-cell frequency may represent cytomegalovirus-driven CD8 T-cell expansions.[22] Another observation was the expression of HLA-DR on peripheral aberrant cells of 2 RCDII patients, of whom 1 patient also showed HLA-DR expression on duodenal aberrant cells. Typically, expression of HLA-DR is restricted to APCs, although it has been described on several tumor types such as melanoma,[23] glioma,[24] and breast cancer.[25] Potentially, HLA-DR expression by aberrant cells could lead to the presentation of neoantigens to CD4 T cells, which could constitute a novel treatment option for such patients. Thus, identification of potential tumor neoantigens in RCDII would be an interesting topic for future studies.

In conclusion, our findings provide evidence for substantial intertumoral and intratumoral heterogeneity at phenotypic and transcriptional levels within the RCDII aberrant cell population, and imply that the tissue context may have to be considered for the development of more effective, patient-tailored therapeutic approaches to improve response to treatment in RCDII and EATL.

Materials and Methods

Human Material

This study was approved by the Medical Ethical Committee from Amsterdam UMC, Vrije Universiteit Amsterdam (protocol 2017.077). Signed informed consent was obtained before collection of human material. This study was performed in accordance with the local ethic guidelines and in accordance with the ethical principles from the Declaration of Helsinki.

For single-cell mass cytometry panel 1, fresh small intestinal biopsy specimens (total, n = 12) with paired peripheral blood samples (n = 9) were obtained from adult patients (n = 10) undergoing diagnostic or follow-up gastroduodenoscopy for RCDII. Two patients were included twice. In addition, control fresh small intestinal biopsy specimens (n = 6) with paired peripheral blood samples (n = 6) were obtained from patients with healthy duodenum. For panel 2, fresh small intestinal biopsy specimens (n = 5) with paired peripheral blood samples (n = 5) were obtained from adult patients (n = 5) undergoing diagnostic or follow-up gastroduodenoscopy for RCDII. For all endoscopies, 2–3 biopsy specimens were collected in Hank's buffered salt solution without calcium and magnesium (Gibco, Thermo Fisher Scientific, Waltham, MA). Blood samples were collected in vacutainer sodium anticoagulant heparin tubes (cat. 368886) (Becton Dickinison (BD), Franklin Lakes, NJ).

Isolation of PBMCs From Peripheral Blood

Blood was diluted 2–3 times in phosphate-buffered saline (PBS), layered on 3 mL Ficoll-Amidotrizoate (LUMC Pharmacy, Leiden, The Netherlands), and centrifuged at 2000 rpm for 20 minutes at room temperature (rT) with break zero. The leukocyte layer was collected using a Pasteur pipette, transferred to 20% fetal calf serum (FCS)/RPMI (Gibco, Thermo Fisher Scientific), washed, and resuspended in staining buffer (Fluidigm, San Francisco, CA).

Isolation of Leukocytes From Duodenal Biopsy Specimens

IELs were isolated from 2 to 3 duodenal biopsy specimens by treatment with 5 mL Hank's buffered salt solution with 1 mmol/L EDTA (made in-house; J.T.Baker, Avantor delivered by VWR, Radnor, PA) rolling for 2 $\times$ 45 minutes at 37°C. Cells were collected in 1 mL 20% FCS/RPMI and kept at 4°C. Subsequently, single-cell suspensions were obtained from the LP by 1.5 hours of enzymatic treatment with 10 U/mL collagenase IV (Worthington, Freehold, NJ) and 200 μg/mL DNase I grade II (Roche, Basel, Switzerland). To obtain single cells, LP cells and IELs were resuspended and passed through a 70-μm cell strainer. Cells were washed with 0.5% FCS/Dulbecco's PBS (DPBS) (Gibco, Thermo Fisher Scientific) by centrifuging at 1650 rpm for 10 minutes and resuspended in 1 mL staining buffer (Fluidigm).

Snap-Freezing Biopsy Specimens

Biopsy specimens were snap-frozen in optimal cutting temperature (OCT) compound using ice-cold isopenthane (GPR Rectapur; VWR, Radnor, PA) and stored at -80°C.

Antibodies

Thirty-nine metal-tagged Ab panel, cytometry by time-of-flight (CyTOF; mass cytometry) panel 1: CCR6-^{141}Pr, CCR7-^{159}Tb, CD103-^{155}Gd, CD11b-^{209}Bi, CD11c-^{162}Dy, CD122-^{158}Gd, CD123-^{151}Eu, CD127-^{165}Ho, CD14-^{114}Qdot800 (Invitrogen, Thermo Fisher Scientific), CD15-^{115}In, CD16-^{148}Nd, CD161-^{164}Dy, CD163-^{154}Sm, CD1a-^{142}Nd, CD20-^{163}Dy, CD25-^{149}Sm, CD27-^{167}Er, CD28-^{171}Yb, CD3-^{170}Er, CD38-^{172}Yb, CD4-^{145}Nd, CD45-^{89}Y, CD45RA-^{169}Tm, CD45RO-^{173}Yb, CD5-^{160}Gd, CD56-^{176}Yb, CD69-^{14}4Nd, CD7-^{153}Eu, CD8a-^{146}Nd, CD8b-^{166}Er, c-Kit-^{143}Nd, CRTh2-^{156}Gd, HLA-DR-^{168}Er, IgM-^{150}Nd, KLRG1-^{161}Dy, NKp44-^{147}Sm, NKp46-^{174}Yb, PD-1-^{175}Lu, and TCRgd-^{152}Sm. Preconjugated metal-labeled antibodies were purchased from Fluidigm. Purified antibodies specific for CD103, CD122, CD15, CD20, CD28, CD45RO, CD5, CRTh2, HLA-DR, IgM, NKp46 (BioLegend, San Diego, CA), CD1a (Sony Biotechnology Inc, San Jose, CA), KLRG1 (Miltenyi Biotec, Bergisch Gladbach, Germany), CD8b (eBioscience, Thermo Fisher Scientific), and NKp44 (R&D Systems, Minneapolis, MN) were conjugated in-house with the MaxPar X8 antibody labeling kit (Fluidigm) according to the manufacturer's instruction. Self-conjugated antibodies were validated using OneComp beads (Invitrogen, Thermo Fisher Scientific) and on PBMCs.

Forty-two–metal-tagged Ab panel, CyTOF panel 2: CCR6-^{141}Pr, CCR7-^{159}Tb, CD103-^{155}Gd, CD11c-157Gd, CD122-^{158}Gd, CD127-^{165}Ho, CD161-^{164}Dy, CD19-142Nd, CD25-^{149}Sm, CD27-^{167}Er, CD28-^{171}Yb, CD3-^{170}Er, CD38-^{172}Yb, CD4-^{145}Nd, CD45-^{89}Y, CD45RA-^{114}Qdot645 (Invitrogen, Thermo Fisher), CD45RO-^{173}Yb, CD56-^{176}Yb, CD57-^{194}Pt, CD69-^{144}Nd, CD7-^{153}Eu, CD8a-^{146}Nd, CD8b-^{166}Er, CD95-^{209}Bi, c-Kit-^{143}Nd, Eomes-^{163}Dy, FoxP3-^{162}Dy, GATA3-^{169}Tm, Helios-^{168}Er, HLA-DR-^{198}Pt, ICOS-^{151}Eu, ILT2/LILRB1-^{156}Gd, KLRG1-^{161}Dy, NKp44-^{147}Sm, PD-1-^{175}Lu, Perforin-^{150}Nd, RORgt-^{174Yb}, T-bet-^{160}Gd, TCRgd-^{152}Sm, transforming growth factor (TGF)-β-^{115}In, TIGIT-^{148}Nd, and TIM3-^{154}Sm. Preconjugated metal-labeled antibodies were purchased from Fluidigm. Purified antibodies specific for CD103, CD11c, CD122, CD28, CD45RO, CD57, CD95, Helios, HLA-DR (BioLegend), RORgt (BD), TGF-b (Bio-Rad Laboratories, Hercules, CA), CD8b, Eomes (eBioscience, Thermo Fisher Scientific), GATA3, KLRG-1 (Miltenyi Biotec, Bergisch Gladbach, Germany), NKp44 (R&D systems), Perforin (MyBioSource, San Diego, CA), and TIGIT (Invitrogen, Thermo Fisher Scientific, Waltham, MA) were conjugated in-house as previously described.

Forty-metal-tagged Ab panel, imaging CyTOF panel 2: CD103-^{155}Gd, CD117-^{165}Ho, CD11c-^{162}Dy (Fluidigm), CD11c-^{162}Dy (BioLegend), CD123-^{151}Eu, CD127-^{174}Yb, CD138-^{147}Sm, CD141-^{160}Gd, CD16-^{142}Nd, CD161-^{164}Dy, CD163-^{154}Sm, CD19-^{175}Lu, CD1c-^{171}Yb, CD20-^{161}Dy, CD27-^{167}Er, CD3-^{170}Er, CD30-^{158}Gd, CD34-^{148}Nd, CD38-^{172}Yb, CD4-^{145}Nd, CD45-^{89}Y, CD45RA-^{169}Tm, CD45RO-^{173}Yb, CD5-^{149}Sm, CD56-^{176}Yb, CD66b-^{163}Dy, CD68-^{159}Tb, CD69-^{144}Nd, CD7-^{153}Eu, CD86-^{156}Gd, CD8a-^{146}Nd, D2-40-^{115}In, E-cadherin-^{150}Nd, FCεRIa-^{143}Nd, HLA-DQ-^{141}Pr, HLA-DR-^{168}Er, Ki67-^{166}Er, SMA-^{194}Pt, TCRgd-^{152}Sm, and vimentin-^{198}Pt. Preconjugated metal-labeled antibodies were purchased from Fluidigm. Purified antibodies specific for CD103 (Abcam, Cambridge, UK), CD127 (Beckman Coulter, Brea, CA), CD117, CD11c, CD138, CD141, CD16, CD19, CD1c, CD45RO, CD5, CD66b, D2-40, FCεRIa, HLA-DR (BioLegend), HLA-DQ (in-house) E-cadherin, Ki67, SMA, vimentin (Cell Signaling Technology, Danvers, MA), CD30 (Dako Omnis, Agilent, Santa Clara, CA), TCRgd (eBioscience, Thermo Fisher Scientific), CD34 and CD56 (Thermo Fisher Scientific) were conjugated in-house as previously described.

Single-Cell Mass Cytometry

After single-cell isolation, cells were washed with staining buffer (Fluidigm) (with 1:250 diluted in 0.5 mmol/L EDTA) and incubated with 1 mL 1:2000 diluted 2000 mmol/L intercalator-103Rh (Fluidigm) for 15 minutes at rT for identification of dead cells. After washing and $\geq$ 10 minutes of incubation with Fc receptor blocking solution (BioLegend), cells were stained with metal-conjugated antibodies for 45 minutes at rT. After staining, cells were washed 3 times with staining buffer. For identification of nucleated cells, cells were labeled with 1 mL 1:4000 diluted 500 mmol/L Cell-ID Intercalator-Ir (Fluidigm) in MaxPar Fix and Perm buffer (Fluidigm) at 4°C overnight, for up to 48 hours. After incubation, cells were washed 3 times with staining buffer at 2500 rpm for 5 minutes. Before the final wash, cells were counted to adjust cell concentrations for measurement.

Within 14 days, samples were acquired at Helios mass cytometer (Fluidigm) with the narrow-bore injector at the Flow Core Facility (FCF) of the LUMC. Samples were concentrated in MilliQ, and EQ Four Elements Calibration beads (Fluidigm, passport number EQ-P13H2302_ver2) were spiked in with each sample in a 1:10 concentration and used for normalization. Samples were measured in batches of 2–8 samples per day, all performed by the same operator. Paired intestinal and blood samples were measured on the same day. After each round of sample measurement at the Helios mass cytometer, fcs.files were bead-normalized and, if necessary, concatenated using onboard CyTOF software.

Single-Cell RNA-Sequencing

IELs and LP cells were isolated from 7 duodenal biopsy specimens per patient, as described earlier. Hereafter, cells were treated with red blood cell lysis buffer (LUMC Pharmacy), and removal of dead cells was performed using microbeads (Miltenyi Biotec). Lastly, live CD45^{+} cells were positively selected using MACS beads (Miltenyi Biotec). scRNA-seq was performed using 10× Genomics Single Cell system (Pleasanton, CA). Samples were sequenced on 1 run with the NovaSeq 6000 system (Illumina, San Diego, CA). Data were preprocessed with Cell Ranger software v2.2.0 from 10X Genomics.

Single-Cell Data Analysis

For analysis of mass cytometry data, FlowJo v10 software (BD) was used for pregating and calculation of single live CD45$^+$ cells, herewith removing duplicates, beads, dead cells, and debris (data not shown). All patient samples were checked for consistency of antibody staining in FlowJo. In panel 1, inconsistency of antibody staining was found for CD8α, CD103, CD20, and IgM (data not shown). At an overview level, all markers were used for clustering and assignment of cells to major lineages. For further Cytosplore analysis, inconsistent Abs were not used for clustering but were shown for marker expression overlays and interpretation of data. In panel 2, we observed inconsistent staining of 7 antibodies, namely CD103, CD8α, TGF-β, CD95, CD57, Helios, and Perforin (data not shown). Antibodies CD57, Helios and Perforin showed a complete shift in staining and were not used for analysis at all. Similar as for the first panel, inconsistent markers were not used for clustering but were shown for marker expression overlays and interpretation of data.

Cytosplore^{+HSNE} was used for further analysis.[11,12] In Cytosplore, every sample was given a unique sample tag and arcsine transformation was performed with cofactor 5 simultaneously for each marker, to obtain median marker expression values. For identification of major immune cell lineages, a 5-level HSNE was performed with perplexity 30 (1000 iterations). Cells that ended up in the wrong lineage were transferred to the correct lineage before further analysis. Subsequently, every lineage was analyzed separately using HSNE analysis when consisting of $\geq 0.5 \times 10^5$ cells or tSNE analysis when $\leq 0.5 \times 10^5$ cells in Cytosplore. For cell cluster identification, clusters were defined by at least 100 cells. Bar graphs were generated using GraphPad Prism v8 (San Diego, CA).

For analysis of scRNA-seq data, Seurat package v3.1.1[15] was used in R version 4.0.1. Separate preprocessed data sets were setup in 2 Seurat objects and analyzed in parallel. Next, data were filtered by the criteria that each gene was expressed in 3 or more cells and 200 or more genes were expressed per cell. Second filtering criteria were cells with unique gene cell counts fewer than 200 and more than 5000, and a mitochondrial gene percentage of greater than 15% and greater than 25% for data sets 1 and 2 (RCDII 12, RCDII 4-2), respectively. Filtered data were log-normalized, scaled, and unwanted sources of variation (mitochondrial gene percentage, number of detected molecules per cell) were removed. Principal component analysis (PCA) was performed based on the 2000 most variable genes, selected using the vst method. For both data sets, 18 PCA dimensions were used for graph-based clustering with a resolution of 1.1 and 0.8 for data sets 1 and 2, respectively. Clusters were visualized with a UMAP algorithm. When zooming in, 20 PCA dimensions were used for graph-based clustering. A resolution of 0.6 was used for reclustering of data set 1 (RCDII 12), and a resolution of 0.9 for data set 2 (RCDII 4-2).

Imaging Mass Cytometry

First, performance and dilution of BSA- and carrier-free antibodies was tested by immunohistochemical staining on lymph node or duodenal tissue. Purified, BSA- and carrier-free antibodies were conjugated in-house with the MaxPar X8 antibody labeling kit (Fluidigm) according to the manufacturer's instructions. Self-conjugated antibodies were validated by measurement at the Hyperion imaging mass cytometry system.

Cutting, staining, and measurement of all tissues shown were performed in 1 experiment. Cutting of snap-frozen biopsy specimens was performed using the Leica CM3050 S Research Cryostat (Wetzlar, Germany). Tissue sections of 5 μm were obtained, placed on silane-coated glass slides (VWR), and dried for 30–60 minutes at rT. First, sections were fixated for 5 minutes at rT with 1% paraformaldehyde and placed in DPBS. The second fixation step followed in methanol for 5 minutes at -20°C followed by placement in DPBS. Sections were washed twice with wash buffer (DPBS 0.5%, 0.05% Tween) and rehydrated with DPBS. To decrease nonspecific antibody binding, sections were incubated with Superblock (Thermo Fisher Scientific) for 30 minutes at rT. Sections were stained with diluted primary antibodies (in PBS, 0.5% BSA, 0.05% Tween) and incubated overnight (o/n) at 4°C. Sections were washed and stained with 1:400 DNA-intercalator-IR (500 μmol/L) (Fluidigm) for 30 minutes at rT. Afterward, sections were washed, first pressure air dried, and the air dried for 20 minutes.

Stained tissue sections were acquired within 14 days using the Hyperion mass cytometry system (Fluidigm) at the FCF of the LUMC. Regions of interest (ROIs) were selected based on H&E staining of serial tissue sections. ROIs were ablated with an ablation spot the size of 1 um^2 and a frequency of 200 Hz. Acquired data were exported as MCD files and visualized using a Fluidigm MCD viewer. First, we analyzed single stains per sample (control lymph node, control duodenum, 2 RCDII samples) (1 chosen ROI per sample) (data not shown). Data were analyzed using spectral color analysis in a Fluidigm MCD viewer.

Statistics

Data represented in box plots were presented as medians ± interquartile range. Group comparisons were performed using Mann–Whitney *U* tests (2-tailed) in GraphPad Prism v8.

Data Availability

Single-cell mass cytometry data are available via FlowRepository, identifier FR-FCM-Z4X8. scRNA-seq data are available via the NCBIs Gene Expression Omnibus[26] accession code: GSE195780. The remaining data that support the findings of this study are available from the corresponding author upon reasonable request

References

1. Lebwohl B, Rubio-Tapia A. Epidemiology, presentation, and diagnosis of celiac disease. Gastroenterology 2021; 160:63–75.
2. Lundin KE, Scott H, Hansen T, Paulsen G, Halstensen TS, Fausa O, Thorsby E, Sollid LM. Gliadin-specific, HLA-DQ(alpha 1*0501,beta 1*0201) restricted T cells isolated from the small intestinal mucosa of celiac disease patients. J Exp Med 1993;178:187–196.
3. Cellier C, Patey N, Mauvieux L, Jabri B, Delabesse E, Cervoni JP, Burtin ML, Guy–Grand D, Bouhnik Y, Modigliani R, Barbier JP, Macintyre E, Brousse N, Cerf–Bensussan N. Abnormal intestinal intraepithelial lymphocytes in refractory sprue. Gastroenterology 1998; 114:471–481.
4. Schmitz F, Tjon JML, Lai Y, Thompson A, Kooy-Winkelaar Y, Lemmers RJLF, Verspaget HW, Mearin ML, Staal FJ, Schreurs MW, Cupedo T, Langerak AW, Mulder CJ, van Bergen J, Koning F. Identification of a potential physiological precursor of aberrant cells in refractory coeliac disease type II. Gut 2013;62:509.
5. Ettersperger J, Montcuquet N, Malamut G, Guegan N, Lopez-Lastra S, Gayraud S, Reimann C, Vidal E, Cagnard N, Villarese P, Andre-Schmutz I, Gomes Domingues R, Godinho-Silva C, Veiga-Fernandes H, Lhermitte L, Asnafi V, Macintyre E, Cellier C, Beldjord K, Di Santo JP, Cerf-Bensussan N, Meresse B. Interleukin-15-dependent T-cell-like innate intraepithelial lymphocytes develop in the intestine and transform into lymphomas in celiac disease. Immunity 2016;45: 610–625.
6. Malamut G, El Machhour R, Montcuquet N, Martin-Lannerée S, Dusanter-Fourt I, Verkarre V, Mention J-J, Rahmi G, Kiyono H, Butz EA, Brousse N, Cellier C, Cerf-Bensussan N, Meresse B. IL-15 triggers an antiapoptotic pathway in human intraepithelial lymphocytes that is a potential new target in celiac disease-associated inflammation and lymphomagenesis. J Clin Invest 2010; 120:2131–2143.
7. Perfetti V, Baldanti F, Lenti MV, Vanoli A, Biagi F, Gatti M, Riboni R, Dallera E, Paulli M, Pedrazzoli P, Corazza GR. Detection of active Epstein–Barr virus infection in duodenal mucosa of patients with refractory celiac disease. Clin Gastroenterol Hepatol 2016;14:1216–1220.
8. Cording S, Lhermitte L, Malamut G, Berrabah S, Trinquand A, Guegan N, Villarese P, Kaltenbach S, Meresse B, Khater S, Dussiot M, Bras M, Cheminant M, Tesson B, Bole-Feysot C, Bruneau J, Molina TJ, Sibon D, Macintyre E, Hermine O, Cellier C, Asnafi V, Cerf-Bensussan N. Oncogenetic landscape of lymphomagenesis in coeliac disease. Gut 2022;71:497–508.
9. Soderquist CR, Lewis SK, Gru AA, Vlad G, Williams ES, Hsiao S, Mansukhani MM, Park DC, Bacchi CE, Alobeid B, Green PH, Bhagat G. Immunophenotypic spectrum and genomic landscape of refractory celiac disease type II. Am J Surg Pathol 2021;45:905–916.
10. Al-Toma A, Verbeek WHM, Hadithi M, von Blomberg BME, Mulder CJJ. Survival in refractory coeliac disease and enteropathy-associated T-cell lymphoma: retrospective evaluation of single-centre experience. Gut 2007;56:1373–1378.
11. van Unen V, Hollt T, Pezzotti N, Li N, Reinders MJT, Eisemann E, Koning F, Vilanova A, Lelieveldt BPF. Visual analysis of mass cytometry data by hierarchical stochastic neighbour embedding reveals rare cell types. Nat Commun 2017;8:1740.
12. Höllt T, Pezzotti N, van Unen V, Koning F, Eisemann E, Lelieveldt B, Vilanova A. Cytosplore: interactive immune cell phenotyping for large single-cell datasets. Computer Graphics Forum 2016;35:171–180.
13. Vivier E, Artis D, Colonna M, Diefenbach A, Di Santo JP, Eberl G, Koyasu S, Locksley RM, McKenzie ANJ, Mebius RE, Powrie F, Spits H. innate lymphoid cells: 10 years on. Cell 2018;174:1054–1066.
14. Butler A, Hoffman P, Smibert P, Papalexi E, Satija R. Integrating single-cell transcriptomic data across different conditions, technologies, and species. Nat Biotechnol 2018;36:411–420.
15. Tack GJ, van Wanrooij RLJ, Langerak AW, Tjon JML, von Blomberg BME, Heideman DAM, van Bergen J, Koning F, Bouma G, Mulder CJJ, Schreurs MWJ. Origin and immunophenotype of aberrant IEL in RCDII patients. Mol Immunol 2012;50:262–270.
16. Mention J-J, Ben Ahmed M, Bègue B, Barbe U, Verkarre V, Asnafi V, Colombel J-f, Cugnenc P-h, Ruemmele FM, McIntyre E, Brousse N, Cellier C, Cerf-Bensussan N. Interleukin 15: a key to disrupted intraepithelial lymphocyte homeostasis and lymphomagenesis in celiac disease. Gastroenterology 2003; 125:730–745.
17. Johnson DE, O'Keefe RA, Grandis JR. Targeting the IL-6/JAK/STAT3 signalling axis in cancer. Nat Rev Clin Oncol 2018;15:234–248.
18. Kooy-Winkelaar YMC, Bouwer D, Janssen GMC, Thompson A, Brugman MH, Schmitz F, de Ru AH, van Gils T, Bouma G, van Rood JJ, van Veelen PA, Mearin ML, Mulder CJ, Koning F, van Bergen J. CD4 T-cell cytokines synergize to induce proliferation of malignant and nonmalignant innate intraepithelial lymphocytes. Proc Natl Acad Sci U S A 2017;114:E980.
19. Cellier C, Delabesse E, Helmer C, Patey N, Matuchansky C, Jabri B, Macintyre E, Cerf-Bensussan N, Brousse N. Refractory sprue, coeliac disease, and enteropathy-associated T-cell lymphoma. Lancet 2000;356:203–208.
20. Li M, Yao D, Zeng X, Kasakovski D, Zhang Y, Chen S, Zha X, Li Y, Xu L. Age related human T cell subset evolution and senescence. Immun Ageing 2019;16:24.
21. Czesnikiewicz-Guzik M, Lee W-W, Cui D, Hiruma Y, Lamar DL, Yang Z-Z, Ouslander JG, Weyand CM, Goronzy JJ. T cell subset-specific susceptibility to aging. Clin Immunol 2008;127:107–118.
22. Khan N, Shariff N, Cobbold M, Bruton R, Ainsworth JA, Sinclair AJ, Nayak L, Moss PAH. Cytomegalovirus seropositivity drives the CD8 T cell repertoire toward greater clonality in healthy elderly individuals. J Immunol 2002;169:1984.

23. Pollack MS, Heagney SD, Livingston PO, Fogh J. HLA-A, B,C and DR alloantigen expression on forty-six cultured human tumor cell lines2. J Natl Cancer Inst 1981; 66:1003–1012.
24. Carrel S, De Tribolet N, Gross N. Expression of HLA-DR and common acute lymphoblastic leukemia antigens on glioma cells. Eur J Immunol 1982;12:354–357.
25. Bártek J, Petřek M, Vojtěšek B, Bártková J, Kovařík J, Rejthar A. HLA-DR antigens on differentiating human mammary gland epithelium and breast tumours. Br J Cancer 1987;56:727–733.
26. Edgar R, Domrachev M, Lash AE. Gene Expression Omnibus: NCBI gene expression and hybridization array data repository. Nucleic Acids Res 2002;30:207–210.

Received November 25, 2021. Accepted March 15, 2022.

Correspondence
Address correspondence to: Frits Koning, PhD, Department of Immunology, Leiden University Medical Center, Building 1, Albinusdreef 2, 2223 ZA Leiden, The Netherlands. e-mail: f.koning@lumc.nl; fax: +31(0)715265267.

Acknowledgments
The authors thank all patients for participating in this study. The authors thank all gastroenterologists and endoscopy nurses for performing endoscopies and obtaining patient samples. The authors thank Knut E. A. Lundin for flying to Amsterdam to provide patient samples. The authors thank the FCF of LUMC for technical support during mass cytometric measurements. The authors thank the Leiden Genome Technology Center for their help with scRNA-seq.

CRediT Authorship Contributions
Tessa Dieckman (Conceptualization: Equal; Data curation: Lead; Formal analysis: Lead; Investigation: Lead; Methodology: Equal; Project administration: Lead; Resources: Equal; Visualization: Lead; Writing – original draft: Lead)
Mette Schreurs (Investigation: Supporting)
Ahmed Mahfouz, PhD (Data curation: Supporting; Formal analysis: Supporting)
Yvonne Kooy-Winkelaar (Investigation: Supporting)
Andra Neefjes-Borst (Formal analysis: Supporting)
Gerd Bouma, PhD (Project administration: Lead; Resources: Lead; Supervision: Equal; Writing – review & editing: Equal)
Frits Koning, PhD (Conceptualization: Lead; Funding acquisition: Lead; Methodology: Lead; Supervision: Lead; Visualization: Equal; Writing – original draft: Equal; Writing – review & editing: Lead)

Conflicts of interest
The authors disclose no conflicts.

Funding
This research was supported by the KWF Dutch Cancer Society (UL 2015-2850) and by collaboration project TIMID (LSHM18057-SGF), financed by the public–private partnership allowance made available by Top Sector Life Sciences and Health to Samenwerkende Gezondheidsfonden, to stimulate public-private partnerships and co-financing by health foundations that are part of the Samenwerkende Gezondheidsfonden.

Data Transparency
Single-cell mass cytometry data are available via FlowRepository, identifier FR-FCM-Z4X8. Single-cell RNA-seq data are available via the NCBI Gene Expression Omnibus, accession code: GSE195780. The remaining data that support the findings of this study are available from the corresponding author upon reasonable request.